Near Field Radio Holography of the ALMA Prototype Antennas

Jacob W. M. Baars (ESO), Robert Lucas (IRAM), and Jeff Mangum (NRAO)

December 1, 2004

Contents

1 Summary

We summarise the mathematical foundation of the holographic method of measuring the reflector profile of an antenna or radio telescope. In particular, we treat the case, where

the signal source is located at a finite distance of the antenna under test, necessitating the inclusion of the so-called Fresnel field terms in the radiation integrals. We assume a "full phase" system with reference receiver to provide the reference phase. Thus so-called phase-recovery schemes are not discussed here. These have been extensively described by Morris (1985).

Then we describe in some detail the hardware and software implementation of the system used for the holographic measurement of the ALMA prototype antennas at the VLA site. We include a description of the practicalities of a measurement and surface setting. Finally, we present the holographic measurement results for both the VertexRSI and AEC (Alcatel-EIE-Consortium) prototype ALMA antennas.

2 Introduction

Large reflector antennas, as those used in radio astronomy and deep-space communication, generally are composed of a set of surface panels, supported on three or more points by a support structure, often called the backup structure. After assembly of the reflector it is necessary to accurately locate the panels onto the prescribed paraboloidal surface in order to obtain the maximum antenna gain. The fact that some antennas have a "shaped" contour is irrelevant for the purpose of our discussion. We are concerned with describing a method which allows us to derive the position of the individual panels in space and compute the necessary adjustments of their support points to obtain a continuous surface of a certain prescribed shape.

The analysis by Ruze (1966) of the influence of random errors in the reflector contour on the antenna gain indicates that the rms error should be less than about one-sixteenth of the wavelength for acceptable performance. Under the assumption that the errors are randomly distributed with rms value ϵ and have a correlation length $\mathbf{c}$ which is much larger than the wavelength λ and much smaller than the reflector diameter D, the relative decrease in aperture efficiency (or gain) can be expressed by the simple formula

$$\frac{\eta_A}{\eta_{A0}} = \exp\left\{-\left(\frac{4\pi\epsilon}{\lambda}\right)^2\right\}, \tag{1}$$

where η_{A0} is the aperture efficiency of the perfect reflector. An error of $\lambda/40$ is required to limit the gain loss to 10 percent.

The first large reflectors for radio astronomy, here also called radio telescope, had a diameter of about 25 m and operated at wavelengths longer than 10 cm. Thus a surface precision of several millimeters would have provided excellent performance. A measurement accuracy of this order-of-magnitude is readily achievable with a classic "theodolite and tape" method. Using the best theodolites (T3), accuracies of the order of 100 micrometers have been achieved on reflectors of a size up to 30 m (Greve , 1986). However, the development of the technology of large and simultaneously highly accurate antennas has been a very active field over the last 30 years, whereby the application of the design principle of homology (von Hoerner , 1967) has enabled the construction of, for instance, a 100 m diameter radio telescope with a surface accuracy of about 0.5 mm (Hachenberg *et al.*

, 1973; Godwin *et al.* , 1986), a 30 m millimeter telescope with 75 μm accuracy (Baars *et al.* , 1987, 1994) and 10-12 m diameter submillimeter telescopes with an rms surface error of less than 20 μm (*e.g.* Baars *et al.* , 1999). The setting of the reflector panels at such high accuracy has required the development of measuring methods of hitherto unsurpassed accuracy. It should be noted that these measurements need to be done "in the field", which in the case of millimeter radio telescopes often means the hostile environment of a high mountain site.

A number of special measuring methods and devices have been developed (for a review, see Baars , 1983). The most versatile, and by now widely used method is normally called "radio holography". The method makes use of a well-known relationship in antenna theory: the far-field radiation pattern of a reflector antenna is the Fourier Transformation of the field distribution in the aperture of the antenna. Note that this relationship applies to the amplitude and phase distributions, not to the power pattern. Thus, if we can measure the radiation pattern, *in amplitude and phase*, over a sufficiently large angular area, we can derive by Fourier Transformation the amplitude and phase distribution in the antenna aperture plane with an acceptable spatial resolution. The latter is determined by the angular size of the measured radiation pattern. This method was suggested, but not worked out in any detail, in the appendix of Jennison's pocket book "Radio Astronomy" (Jennison , 1966). The paper by Bennett *et al.* (1976) presented a sufficiently detailed analysis to draw the attention of radio astronomers. Thus, Scott & Ryle (1977) used the new Cambridge 5 km array to measure the shape of four of the eight antennas, using a celestial radio point source and the remaining antennas to provide the reference signal.

The use of a natural, celestial signal source is very attractive for two reasons. First the source is definitely in the far-field of the antenna. The **far-field region** of the antenna is defined to start at

$$R_f = \frac{2D^2}{\lambda}, \tag{2}$$

and can easily reach values of several hundreds of kilometers. Thus no earth-bound transmitter will ever be in the far-field for these applications. Secondly, the celestial radio source traces a daily path across the sky, providing a range of elevation angles over which the data can be collected. This is of great interest for the study of elevation dependent deformations of the antenna, caused by gravity. However, normally the intensity of the cosmic source is not sufficient to achieve the required signal-to-noise ratio for an accurate measurement. Only a few strong sources are available. The situation is more favourable if there are several large antennas, as in interferometric arrays, where the extra antennas can be used to provide a strong reference signal.

For the IRAM 30 m millimeter telescope on Pico Veleta (Baars *et al.* , 1987) it was decided to use a holographic system at 22 GHz, using the giant water vapour maser in the Orion Nebula, which flared to an intensity of several million jansky during the design phase of the telescope. The reference signal was provided by a 1.5m diameter reflector located in the back of the prime-focus cage of the telescope. A compact double receiver in the prime focus served both reference and main reflector. Although by the time of the measurement the maser source had weakened, it was sufficiently strong to enable a measurement of the surface with an accuracy of about 30 μm rms and a setting of the surface to better than

100 μm rms (Morris , 1988).

Artificial satellites, radiating a beacon signal at a fixed frequency can also be used as far-field signal source. Extensive use has been made of synchronous communication satellites in the 11 GHz band (*e.g.* Godwin *et al.* , 1986). These transmitters of course do not provide the range of elevation angles accessible with cosmic sources. Some satellites, notably the LES (Lincoln Experimental Satellite) 8 and 9, have been used for radio holography of millimeter telescopes (*e.g.* Baars *et al.* , 1999). They provided a signal at the high frequency of 37 GHz and with their geo-synchronous orbit moved over some 60 degrees in elevation angle. Unfortunately, both satellites are no longer available. Radio astronomers would be greatly helped if a satellite would become available with a reliable transmitter at a high frequency of about 40, or preferably 95 GHz.

Lacking a sufficiently strong source in the far-field, we have to take recourse to using an earth-bound transmitter. In practice these will be located at a distance of several hundreds of meters to a few kilometers and be at an elevation angle of less than 10 degrees. Clearly, these are in the near-field of the antenna, requiring significant corrections to the received signals. The detailed treatment of this case is presented in this report.

Successful measurements on short ranges have been reported for the JCMT (Hills *et al.* , 2002) and the ASTE antenna of NAOJ. The ALMA prototype antennas (12 m diameter, surface accuracy 20-25μm) have been measured and set with the aid of a transmitter at a distance of 315 m, elevation angle 9 degrees, radiating at a wavelength near 3 mm. We will discuss the results of these measurements in this report.

3 The Mathematics of Radio Holography

The reciprocity theorem describes the equivalency between the characteristics of a transmitting and receiving antenna. Thus both concepts will be used in the following treatment depending on the specific aspect under description. We shall not repeat here the fundamental analysis which leads from Maxwell's equations to the "physical optics" representation of the characteristics of the reflector antenna (see *e.g.* Silver (1949) and Rusch & Potter (1970)). The basic expression, linking the radiation function $f(x, y, z)$ at a point P in space with the field distribution $F(\xi, \eta)$ over the aperture plane of the antenna, is written as (see Figure 1 for the geometry)

$$f(x,y,z) = \frac{1}{4\pi} \int F(\xi,\eta) \frac{e^{-ikr}}{r} \left[\left(ik + \frac{1}{r} \right) \boldsymbol{i_z} \cdot \boldsymbol{r_1} + ik \boldsymbol{i_z} \cdot \boldsymbol{s} \right] d\xi d\eta, \tag{3}$$

where the integration is extended over the aperture area, $k = 2\pi/\lambda$ and the unit vectors are as indicated in Figure 1 (with $\mathbf{s}$ the propagation vector of the wave field in the aperture). This relation assumes that the aperture is large in units of the wavelength. This general expression can be simplified depending on the distance of the field point P from the aperture plane. We discern the so-called far-field region (Fraunhofer diffraction), nearfield region (Fresnel diffraction) and the evanescent wave zone up to a few wavelengths from the reflector. In the last case, which does not concern us here, no approximations are allowed.

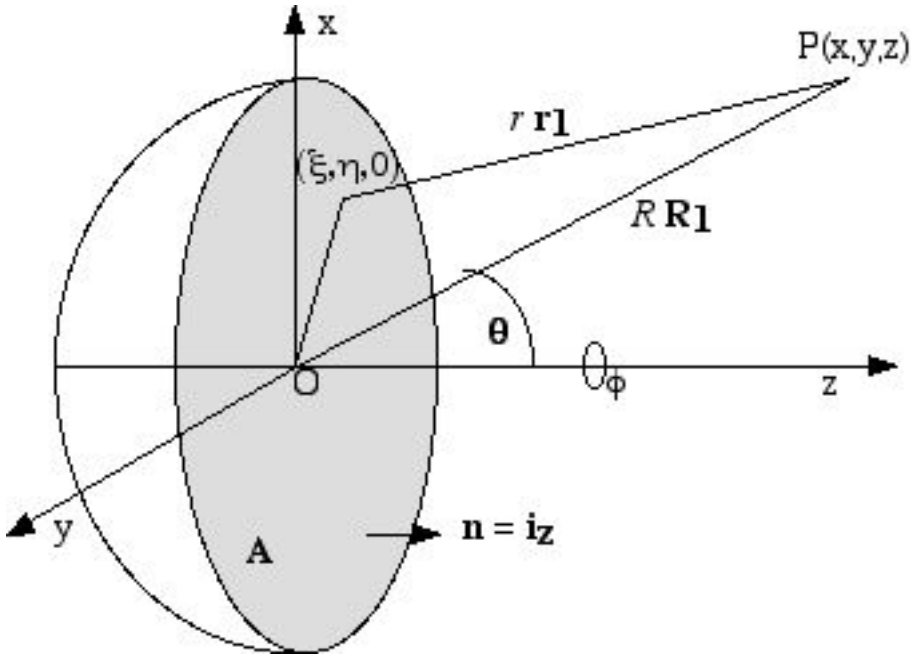

Figure 1: Geometry of the aperture integration method for finite distance to the field point P.

4 The Nearfield Approximation (Fresnel Region)

In the **nearfield** region, which corresponds to the Fresnel region in optical diffraction (see *e.g.* Born & Wolf , 1970) some simplifications can be introduced in the evaluation of Equation 3:

1. r is large enough to ignore its inverse with respect to k in the bracketed term
2. the term 1/r outside the brackets is replaced by the reciprocal distance 1/R from the aperture center to the field point P.
3. the term $\boldsymbol{i_z \cdot r_1}$ can be approximated by $\boldsymbol{i_z \cdot R_1} = \cos\theta$ with R_1 the unit vector from the origin to the field point.
4. the term $\boldsymbol{i_z \cdot s}$ represents a deviation from uniform phase over the aperture. If these are small, this term can be assumed to be equal to one over the aperture.

Note that the variation in r over the aperture must be maintained in the exponent (phase) term. This gives rise to the well-known Fresnel integrals.Thus the nearfield (Fresnel region) expression can be written as

$$f(x,y,z) = \frac{i}{2\lambda R}\int F(\xi,\eta)\left[\cos\theta + 1\right] e^{ikr} d\xi d\eta. \tag{4}$$

We have (see Figure 1)

$$r = \left\{(x-\xi)^2 + (y-\eta)^2 + z^2\right\}^{0.5}. \tag{5}$$

Writing the coordinates of the field point P(x,y,z) in spherical coordinates, we obtain

$$\begin{aligned} x &= R\sin\theta\cos\phi \equiv Ru, \\ y &= R\sin\theta\sin\phi \equiv Rv, \\ z &= R\cos\theta = R\sqrt{(1-u^2-v^2)}, \end{aligned}$$

where we have also introduced the **direction cosines** of the field point

$$P(u, v = \sin\theta\cos\phi, \sin\theta, \sin\phi).$$

Thus, Equation 5 can be written as

$$r = \left\{(Ru-\xi)^2 + (Rv-\eta)^2 + R^2(1-u^2-v^2)\right\}^{0.5} \quad (6)$$

$$= R\left\{1 - 2\frac{u\xi+v\eta}{R} + \frac{\xi^2+\eta^2}{R^2}\right\}^{0.5}. \quad (7)$$

The series expansion of Equation 7 yields

$$r \approx R - (u\xi+v\eta) + \frac{\xi^2+\eta^2}{2R} - \frac{(\xi^2+\eta^2)^2}{8R^3} - \frac{(u\xi+v\eta)^2}{2R} + \frac{(\xi^2+\eta^2)(u\xi+v\eta)}{2R^2} - \ldots \quad (8)$$

Normally, for the Fresnel region analysis, the series is stopped after the quadratic term, which preserves the first three terms of the series in Equation 8. This leads from Equation 4 to the following radiation integral

$$f(u,v) = \frac{i}{\lambda}\frac{e^{ikR}}{R}\int F(\xi,\eta)\exp\left\{ik\left[-(u\xi+v\eta) + \frac{\xi^2+\eta^2}{2R}\right]\right\}d\xi d\eta. \quad (9)$$

The integral of Equation 9 is the well known Fresnel diffraction integral in two coordinates. Considering that for a high gain antenna, the angular region of interest is confined to small values of θ, we can write in Equation 4 $\cos\theta = 1$, which is valid to 0.1 % for angles up to 3 degrees off axis. If we introduce into Equation 9 the spherical coordinates, defined above, and define the aperture as a circular plane with radius **a**, radial coordinate ρ and azimuthal angle χ, the integral takes the form (ignoring the terms before the integral sign)

$$f(\theta,\phi) = \int_0^a\int_0^{2\pi} F(\rho,\chi)\exp\left[ik\left\{-\rho\sin\theta\cos(\chi-\phi) + \frac{\rho^2}{2R}\right\}\right]\rho d\rho d\chi. \quad (10)$$

For a rotationally symmetric aperture distribution $F(\rho)$, independent of χ, the integration over χ results in

$$f(\theta) = 2\pi\int_0^a F(\rho)J_0(k\rho\sin\theta)\exp\left(ik\frac{\rho^2}{2R}\right)\rho d\rho. \quad (11)$$

These integrals have been studied by Lommel in his treatment of Fresnel diffraction at a circular aperture and the solution can be written in terms of Lommel functions (for details *cf.* Baars (1970) or Born & Wolf (1970)).

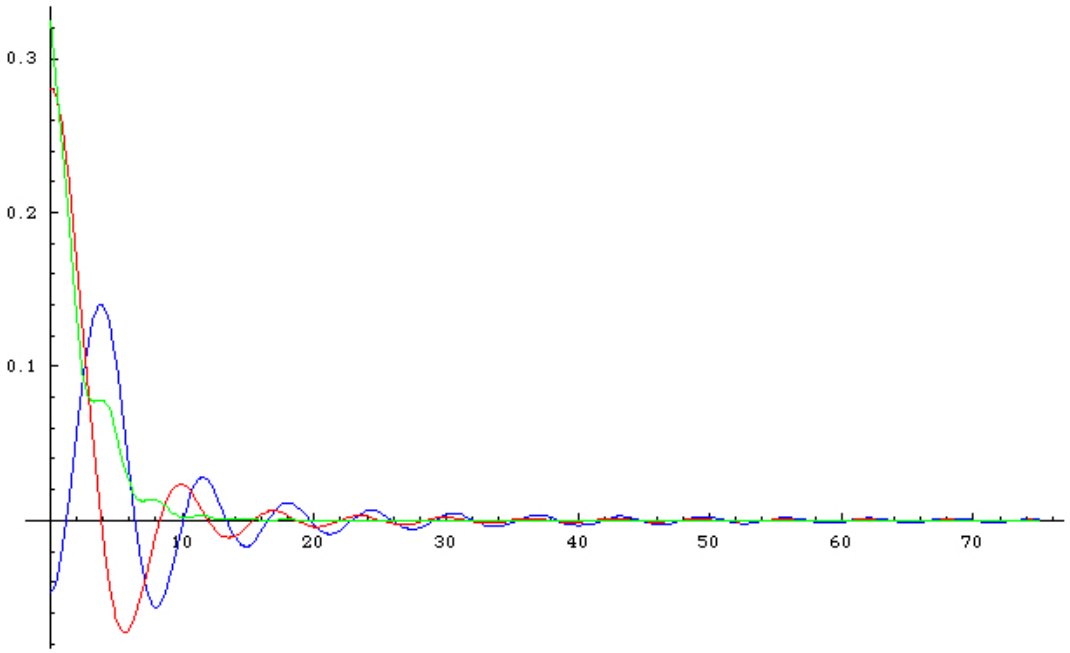

Figure 2: The near-field calculation. Red and blue curves are the sine and cosine-component, respectively, while the green curve is the "powerpattern", i.e. the sum of the squares of the two former (multiplied by a factor 4 for purpose of illustration). This calculation assumes a distance to the aperture of 300 m, wavelength 3 mm and uniform aperture illumination; maximum value of u=75 corresponds with an angle of about 2 degrees off boresight. This numerical example is thus applicable to the holography measurement of the ALMA antennas at the ATF/VLA site.

In the following we illustrate the near-field by numerically integrating Equation 11[1] We assume the aperture function to be of the form $F(\rho) = 1 - (1 - \tau)\rho^2$, the "quadratic on a pedestal τ" illumination function with taper τ (uniform illumination for τ=1). We choose a normalised aperture radius a=1, introduce the variable u=k sin θ and ignore the factor 2π in front of the integration sign. In the integration we must separate the exponent in its cosine and sine part. For uniform illumination, we obtain the result shown in Figure 2.

4.1 The Far-Field Approximation (Fraunhofer Region)

In the **far-field** situation, the field point P is so far away (in principle at infinity) that the vectors $R_1$and $r_1$are parallel and moreover the variation of r in the exponent of Equation 4 can be reduced to the linear form

$$r = R - (u\xi + v\eta) = R - \sin\theta(\xi\cos\phi + \eta\sin\phi). \tag{12}$$

[1]The calculations and resulting plots of Figures 2 through 6 have been made with the aid of the *Mathematica* package. The *Mathematica* expressions are assembled in §B.

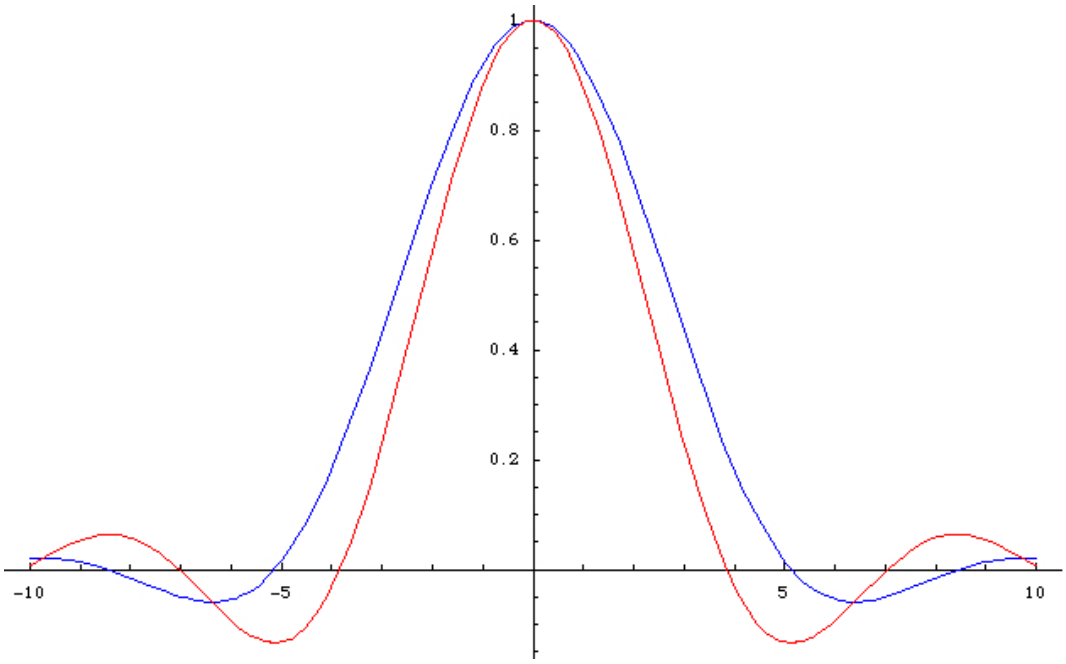

Figure 3: The field pattern for the uniform (red) and fully tapered (blue) illumination function. The tapered case (blue) exhibits a broader beam and lower sidelobes.

Now, the far-field radiation integral, Equation 4 with $\cos\theta = 1$ can be written as

$$f_P(\theta,\phi) = \frac{i}{\lambda}\frac{e^{-ikR}}{R}\int F(\xi,\eta)\exp\left\{ik\sin\theta(\xi\cos\phi+\eta\sin\phi)\right\}d\xi d\eta, \tag{13}$$

where the integration is performed over the aperture A. Again applying this equation to a circular, plane aperture with radius **a** and azimuthal angle χ, the integral is transformed into

$$f(\theta,\phi) = \int_0^a\int_0^{2\pi} F(\rho,\chi)\exp\left[ik\left\{-\rho\sin\theta\cos(\phi-\chi)\right\}\right]\rho d\rho d\chi, \tag{14}$$

which for a rotationally symmetric aperture function $F(\rho)$ takes the form of a Hankel Transform

$$f(\theta,\phi) = 2\pi\int_0^a F(\rho)J_0(k\rho\sin\theta)\rho d\rho \rightarrow 2\pi\frac{J_1(ka\sin\theta)}{ka\sin\theta} = \pi\Lambda_1(ka\sin\theta), \tag{15}$$

where J_0 and J_1 are the Bessel function of the first kind and order zero and one, respectively and Λ_1 is theso-called Lambda function of first order. The expression after the arrow assumes a uniform amplitude distribution $F(\rho) \equiv 1$. Figure 3 presents an illustration of Equation 14 for uniform and tapered illumination.

4.1.1 The Fourier Transformation Relationship

Using the direction cosines (u,v), introduced above after Equation 5, Equation 13 can also be written as

$$f_P(u,v) = \frac{i}{\lambda}\frac{e^{-ikR}}{R}\int F(\xi,\eta)\exp\{ik(\xi u+\eta v)\}d\xi d\eta \tag{16}$$

and we see that there is a fourier transformation relationship between $f(u,v)$ and $F(\xi,\eta)$.

Ignoring the term in front of the integral sign, the **inverse Fourier transformation** can now be written as

$$F(\xi,\eta) = \int f(u,v)\exp\{-ik(u\xi+v\eta)\}dudv, \tag{17}$$

where the integration in principle has to be performed over a closed surface, surrounding the aperture. Thus a knowledge of the entire far-field pattern **both in amplitude and in phase** provides a description of the complex field distribution over the aperture of the antenna, also in amplitude and phase.

It is interesting to note that Silver devotes a lengthy discussion to this relationship (Ch. 6.3, 1949), but concludes that the practical application is limited by the fact that the far-field pattern is only prescribed in power. Thus the phase function of $f(\theta,\phi)$ would be arbitrary and the aperture distribution cannot be uniquely determined. It was, as noted in the introduction, Jennison who mentioned the same relation and its practical usefulness, pointing out that the amplitude and phase can both be measured with an interferometer. When Silver wrote his text in the mid forties, radio interferometry had not yet been developed.

In most cases it will be impossible, or in any case impractical, to measure the far-field pattern over the entire sphere. It can be shown however that a measurement of the pattern out to an angle $\Theta = \mathrm{n}\ \Theta_A$ from the beam axis yields the aperture distribution with a spatial resolution of $\delta = \frac{D}{n}$, where $\Theta_A \approx \frac{\lambda}{D}$ is the half-power beam width and D is the aperture diameter, λ the wavelength.

5 Mathematical Details of Near-Field Holography

We now continue with the treatment of holography in the nearfield. Because we want to derive the complex aperture distribution form the measured near-field pattern, the inverse Fourier Transformation of Equation 4 will be our point of departure, where Equation 5, but now written with direction cosines(u,v), is the expression for the finite distance from a point in the aperture to the field point P. Thus we have the inverse of Equation 4

$$F(\xi,\eta) = \frac{i}{\lambda R}\int f(u,v)\exp(-ikr)dudv. \tag{18}$$

Note that we have assumed that the angle θ is small enough to allow cos θ to be set to unity (<0.1 percent error for θ up to 3 degrees). R is the distance from the antenna aperture center to the holography signal source.

From the discussion in the foregoing section we repeat here the series expansion for the distance **r** (Equation 8):

$$r \approx R - (u\xi + v\eta) + \frac{\xi^2 + \eta^2}{2R} - \frac{(\xi^2 + \eta^2)^2}{8R^3} - \frac{(u\xi + v\eta)^2}{2R} + \frac{(\xi^2 + \eta^2)(u\xi + v\eta)}{2R^2}. \qquad (19)$$

As noted above, normally for the Fresnel region analysis, the series is stopped after the quadratic term, which preserves the first three terms in Equation 19. Here, we shall maintain the next terms too in order to make an estimate of the error in the approximation. Substitution of Equation 19 into Equation 18 yields

$$F(\xi, \eta) = \frac{i}{\lambda} \frac{e^{-ikR}}{R} \exp\{-ik\delta p_1(\xi, \eta)\} \int f(u, v) \exp\{ik(u\xi + v\eta)\} e^{-ik\epsilon} du dv. \qquad (20)$$

The terms in Equation 19, which are independent of the integration variables, have been brought outside the integral under the variable δp_1. The other terms in higher powers of (u,v) are collected under the variable ϵ. They "modify" the direct Fourier Transformation of Equation 20. The first pathlength term

$$\delta p_1(\xi, \eta) = \frac{\xi^2 + \eta^2}{2R} - \frac{(\xi^2 + \eta^2)^2}{8R^3} \qquad (21)$$

causes a rapidly varying phase variation over the aperture, which can be compensated to a large degree by an axial displacement of the feed. A focus adjustment δf away from the reflector causes a path length variation of

$$\delta p_2(\xi, \eta) = \left\{ \xi^2 + \eta^2 + \left(f - \frac{\xi^2 + \eta^2}{4f} + \delta f \right)^2 \right\}^{0.5} - \left\{ f + \frac{\xi^2 + \eta^2}{4f} + \delta f \right\}. \qquad (22)$$

In Figure 4 we illustrate the behaviour of these terms as function of the radial aperture coordinate. The "cosine component" of the phase function of Equation 21 for 3mm wavelength and a distance R = 300 m is shown in red, while the phase function of Equation 22 for a certain choice of δf is superposed in blue. The difference between both terms is shown in the lower plot. Clearly, the phase error increases its spatial frequency for increasing radial aperture coordinate. The difference plot shows that the residuals are significant for the outer half of the aperture. By varying the value of δf, one can obtain an impression of its influence on structure and magnitude of the difference function (Figure 5).

We want to minimise the sum of the two terms (Equations 21 and 22) by choosing the appropriate value of δf. Because of the (ξ,η)-dependence (as shown above), there will be a residual path length error, which we must apply to the result of the Fourier Transformation. A value of 102 mm seems the most useful for R = 300 m. The remaining error must be introduced in the mathematical analysis of the data according to the curve. This is a correction to the aperture phase distribution, obtained after the Fourier Transformation of the measured beam pattern.

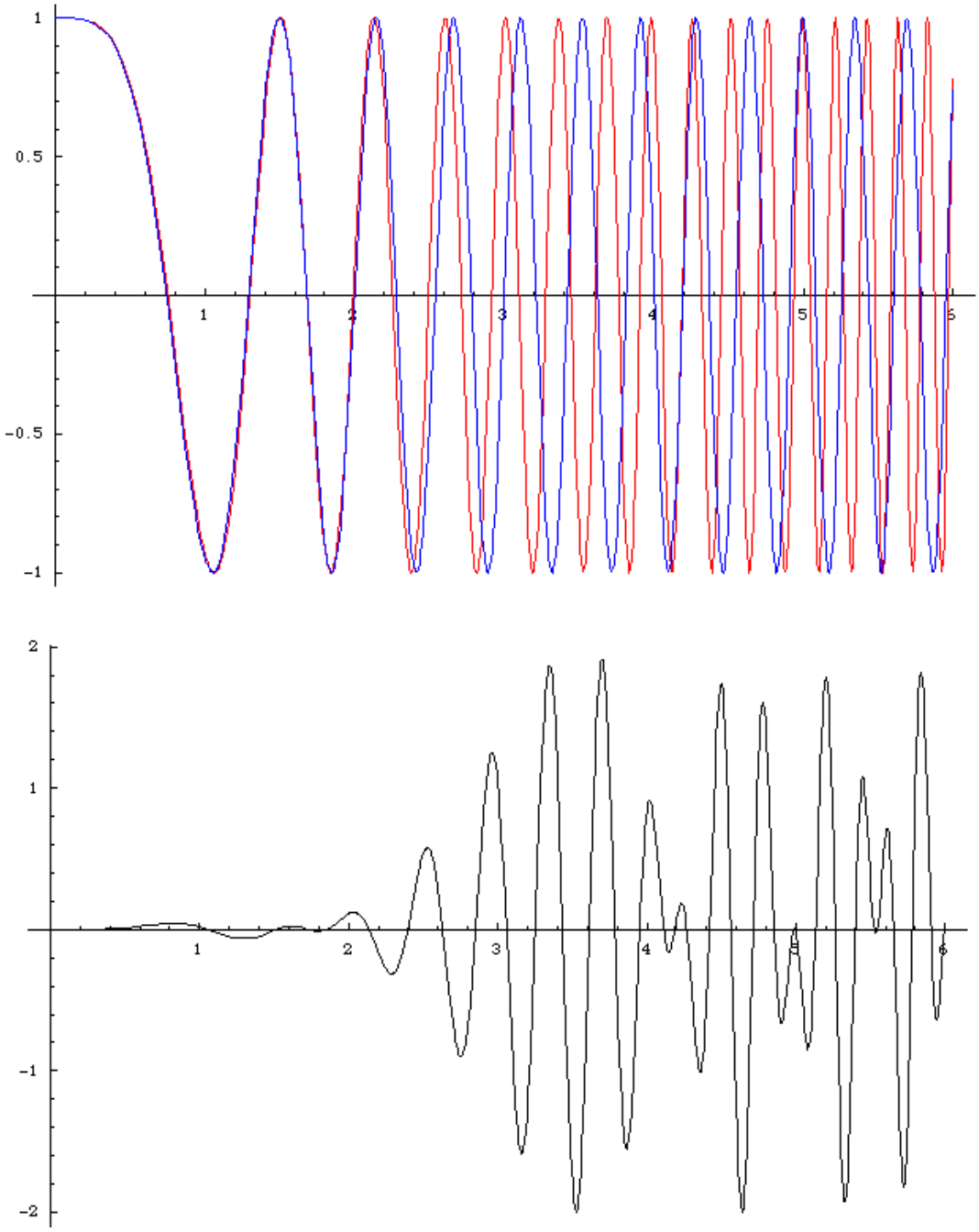

Figure 4: Residual aperture phase for finite distance and axial defocus. Top: Eq.(20), red, and Eq.(21), blue. The lower curve shows the differenceof the two.

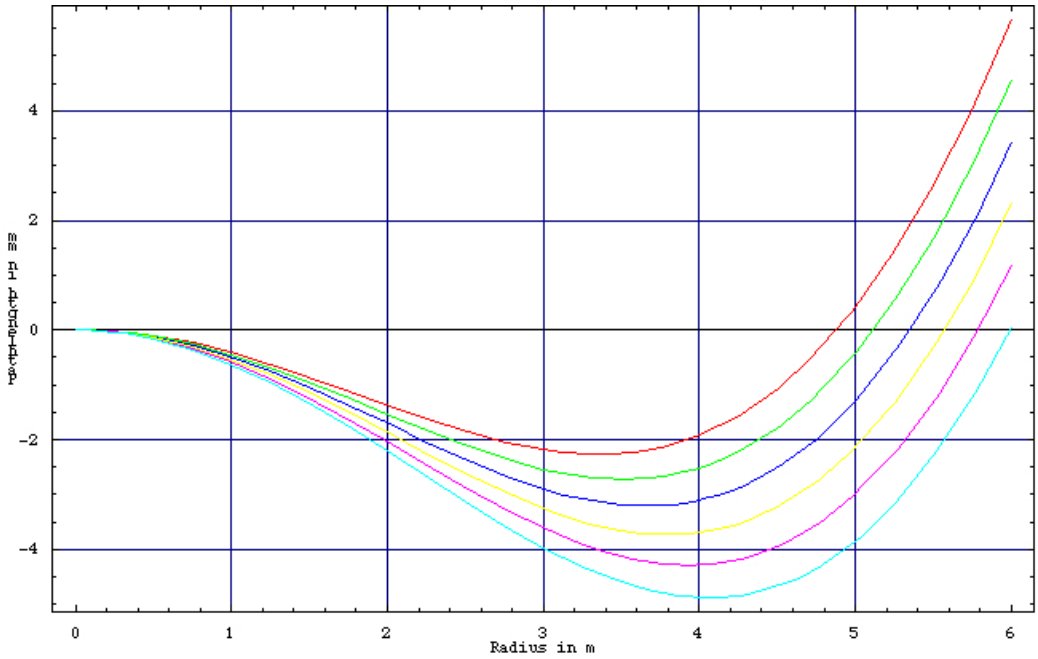

Figure 5: The residual pathlength error in mm for a distance R = 300 m to the holography transmitter and the ALMA 12-m diameter antenna with $\frac{f}{D} = 0.4$. The parameter is the axial defocus δf = 96, step 2, 106 mm, from top to bottom.

The higher order terms in Equation 19, containing the integration variables (u,v), must be discussed separately. They constitute a small pathlength error

$$\epsilon = \frac{\left(\xi^2 + \eta^2\right)(u\xi + v\eta)}{2R^2} - \frac{(u\xi + v\eta)^2}{2R}, \tag{23}$$

which adds a phase term to the integral of Equation 18 of the following form

$$\exp(-ik\epsilon) \approx 1 - ik\epsilon = 1 - ik\left\{u\frac{\xi(\xi^2+\eta^2)}{2R^2} + v\frac{\eta(\xi^2+\eta^2)}{2R^2} - u^2\frac{\xi^2}{2R} - v^2\frac{\eta^2}{2R} - uv\frac{\xi\eta}{R}\right\}. \tag{24}$$

It is seen that this correction involves the calculation of five additional integrals, which look like Fourier Transformations, but aren't really *bona fide* FTs.

The magnitude of the remaining term ϵ (Equation 23) is illustrated in Figure 6.

At the edge of the measured beam the largest path length error is about -0.4 mm at one edge of the aperture. Let us look at some other numerical values for the case of the ALMA antennas. Here the distance R = 300 - 315 m; the reflector diameter is 12 m, so maximum value of (ξ , η) = 6 m. For a beam map with 180 points across a scan, we obtain a resolution in the aperture of about 15 cm, which is fully suitable for the interpolation of the adjuster settings. The scan angle in this case is about plus and minus 1.5 degrees. This means the maximum value of the direction cosines (u,v) $\approx$ 0.03.

Thus the maximum value of the components of Equation 21 become

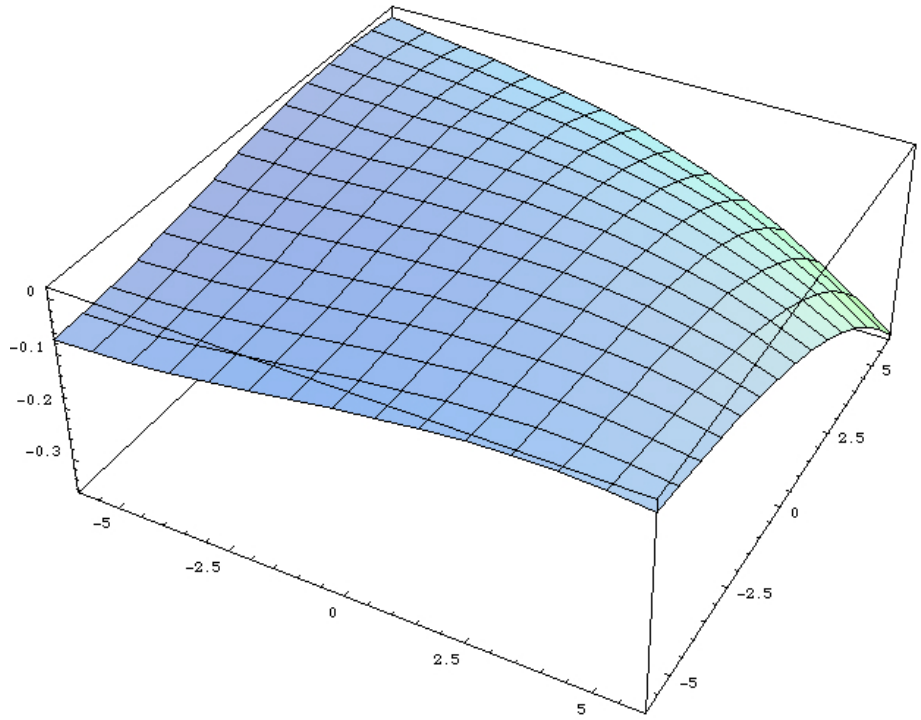

Figure 6: A three-dimensional illustration of the second order path error corrections (Equation 23).

$$\begin{aligned} \delta p_1 &= \frac{72}{600} - \frac{(72)^2}{(8 * (300)^3)} \\ &= 0.12 - 0.24 \times 10^{-4}. \end{aligned}$$

The last term is 5000 times smaller than the first and normally fully negligible. The maximum magnitude of ϵ is

$$\begin{aligned} \epsilon &= \frac{72 * 0.36}{(2 * (300)^2)} - \frac{(0.36)^2}{600} \\ &= 14 \times 10^{-5} - 21.6 \times 10^{-5} \\ &= -8 \times 10^{-5}. \end{aligned}$$

Compare this term with the main term in the Fourier transform (uξ+vη) (Equation 18), which attains a maximum value of 0.36, *i.e.* 4500 times larger.

Nevertheless, because these terms influence the phase over the aperture, they must be dealt with carefully. When all the integrals of Equation 23 are evaluated, it turns out that the contribution of ϵ to the phase amounts to 2 μm pathlength over most of the aperture, reaching a value of 5μm at the edge[2]. In a high accuracy measurement, where the aim is

[2]This is shown in Figure 7.

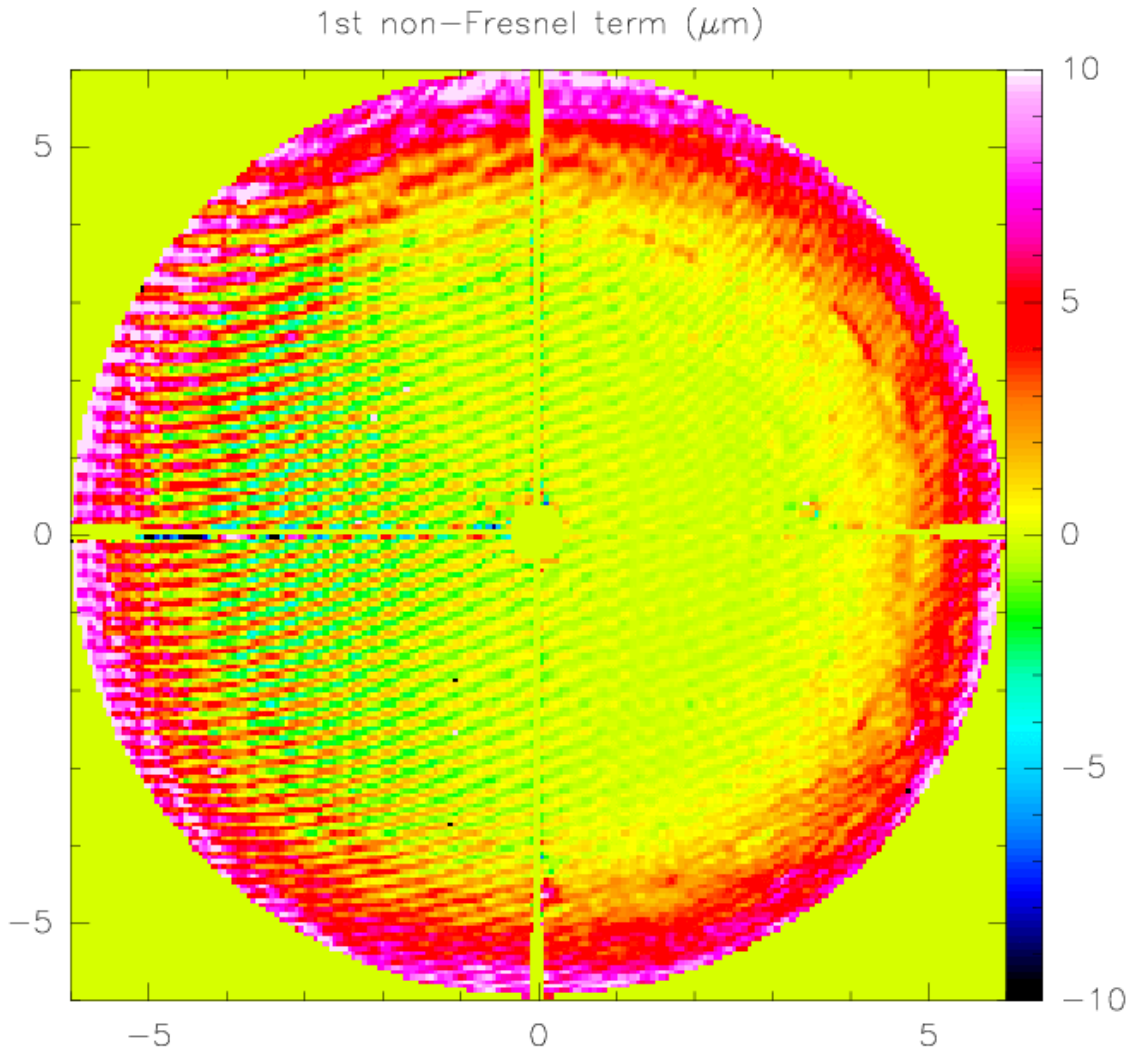

Figure 7: Non-Fresnel correction terms.

to achieve a measuring accuracy of better than 10 μm, one might indeed correct for this term.

As stated above, the near-field path length error of Equation 21 is compensated as well as possible by an axial defocus of the feed (Equation 22). The remaining path error, as depicted, attains values of several millimeters and a correction over the aperture must be applied in all cases. As mentioned earlier, this is easily done by direct addition to the derived aperture distribution after the Fourier Transformation.

It is possible that during the measurement the receiver feed is not located in the optimum refocused position. The pathlength error caused by an axial defocus of δz follows from Equation 22 as

$$\delta p_z = \delta z \left\{ 1 - \frac{1 - \frac{\xi^2+\eta^2}{4f^2} + \frac{\delta f}{f}}{\sqrt{\frac{\xi^2+\eta^2}{4f^2} + \left(1 - \frac{\xi^2+\eta^2}{4f^2} + \frac{\delta f}{f}\right)^2}} \right\}, \tag{25}$$

while a transverse (lateral) offset by an amount δx will cause a pathlength variation of

$$\delta p_x = \delta x \frac{\xi}{f} \left\{ \frac{1}{1+\frac{\delta f}{f}} - \frac{1}{\sqrt{\frac{\xi^2+\eta^2}{f^2} + \left(1 - \frac{\xi^2+\eta^2}{4f^2} + \frac{\delta f}{f}\right)^2}} \right\}. \tag{26}$$

In the reduction process of the holography data, these terms are found by a fit of the measured beam map. The final map of surface deviations is then referred to a position of the feed in the fitted "out-of-focus" location.

6 Practical Realisation of the Holography Measurements

6.1 Task

In this chapter we describe the way in which a holography measurement has been executed on the ALMA prototype antennas at the VLA site. The specification requires the antennas to have a surface accuracy of 25μm RMS for the AEC antenna (with a goal of 20μm) and 20μm for the VertexRSI antenna. ALMA assumed the task to demonstrate this with the aid of a holography system at 3 mm wavelength after delivery of the antennas by the contractors with a surface accuracy of not worse than 100μm RMS. This initial setting was performed by VertexRSI with digital photogrammetry and by AEC with the aid of a Leica "total station" laser-tracker (basically a theodolite with integrated distance measurement instrument and all-electronic readout).

The holography system was designed to provide a measurement repeatability of 10μm, which would suffice to demonstrate the realism in the obtained overall surface accuracy. It should be noted that in the current setup the holography system provides a surface map at one elevation only. No information on the gravitational deformation of the antenna with varying elevation angle can be obtained.

6.2 Equipment and Execution of the Measurement Program

- The signal source for the holography measurements is a monochromatic transmitter at a frequency of 78.92 or 104.02 GHz, located on a 50 m high tower at a distance of 315 and 302 m from the Vertex and AEC antenna, respectively.

- The elevation angle is approximately 8 degrees. The receiver is a full-phase double-receiver, located in the apex region behind the primary focus of the main antenna. The reference signal is received by a wide beam horn pointing along the boresight towards the transmitter.

- Amplitude and phase maps of the antenna beam were obtained by raster scanning. After Fourier Transformation a map of the aperture amplitude and phase distribution was obtained with a spatial resolution over the aperture of about 0.15 m. A typical measurement takes about one hour of time.

- From the phase distribution, which is a representation of the misalignment of the 264 (VertexRSI) or 120 (AEC) panels constituting the reflector, the necessary adjustments of the 5 support points per panel were derived. These were then applied by hand with a simple tool to improve the accuracy of the reflector surface.

The algorithms and software used for the data analysis and derivation of the panel adjustments have been applied successfully at the telescopes of IRAM. The necessary corrections for the finite distance to the transmitter (the "near field" corrections) in our case were derived and checked against similar corrections applied by others, *e.g.* for the JCMT.

The equipment has been designed to provide sufficient signal–to–noise ratio to render the error due to noise insignificant. The greatest risk in this type of measurements lies in undetected or poorly corrected systematic errors.

- An accurate knowledge of the amplitude and phase function of the feedhorn, illuminating the reflector, is essential, because errors in these are fully transferred to the aperture phase map and hence to the surface profile.

- Multiple reflections from the ground or structures form a possible source of errors in this type of work. We carefully covered all areas of potentially harmful reflections with absorbing material. In some controlled experiments we could not demonstrate the existence of reflections.

- The dynamic range of the receiver must be sufficient to accommodate the strong signal on the peak of the beam and the very weak signals towards the edge of the scan. There might have been some saturation on some of the measurements. We discuss this in more detail below.

- The effect of the finite distance of the transmitter can be removed to a large extent (but not completely) by an axial shift in the position of the feed. An error in the distance to the transmitter thus can be corrected in the data analysis by a small adjustment of the feed position. The remaining phase error can be accurately calculated and applied to the data.

6.3 Holography System Hardware

The hardware specifications and requirements are summarised in Tables 1 and 2. In the following we briefly describe the hardware components that comprise the holographic measurement system.

6.3.1 Frontend

The frontend (see Figure 8) is enclosed in a small, temperature controlled box with a diameter of about 30 cm and a length of 50 cm. It fits inside the "apex structure" behind the primary focus of the VertexRSI antenna. The AEC antenna does not provide such a wide space and the receiver is bolted to the outside flange of the apex structure with a long

Table 1: Holography Hardware Requirements

Measurement Error	$< 10\mu$m
Phase Accuracy	$< 0.3^\circ$ ($2.5\mu m$ @ 3mm) RMS
Amplitude Accuracy	$< 1\%$
Dynamic Range	$\geq$ 43dB
Signal-to-Noise Ratio (SNR)	$\geq$ 40dB
Channel-to-Channel Isolation	$>$ 100dB
Date Rate	$\sim$ 80 samples/second (12 msec sampling)

Table 2: Holography Hardware Specifications

Frequencies	78.92 and 104.02 GHz
Frequency Stability	$\leq \pm 5$ Hz/day
Receiver Bandwidth	10 kHz
Receiver Tunability	130 MHz
Transmitter Antenna Gain	33dB
Transmitter EIRP	$> 20\mu$W
Transmitter Power to Antenna	$>$ 10nW
Transmitter Antenna Beam Width @ $-$3dB	4.6° (twice antenna angle at xmtr)
Reference Antenna Beam Width @ $-$3dB	4.6° (twice scan range)
Main Feed Beam Width @ $-$3dB	128° ($-$3dB edge taper)
System Temperature	3200 K
Reference Feed Power Received (P_r)	$1.736 \times 10^{-9} P$
On-Boresight Signal (M_0)	$4.167 \times 10^{-7} P$
On-Boresight Noise (σ_0)	$(1.23 \times 10^{-22} W(P))^{\frac{1}{2}}$
Off-Boresight Noise (P_r Term)	$(2.13 \times 10^{-27} W(P))^{\frac{1}{2}}$
Average map noise for complex correlator (σ_{av})	$(2.23 \times 10^{-25} W(P))^{\frac{1}{2}}$

piece of waveguide bringing the signal feed in focus. Both the signal– and reference–receiver are housed "back-to-back" in this box. This provides a compact system in which the LO signals can easily be made equal in length, greatly contributing to the phase stability of the system. Broadband mixers at ambient temperature convert the received signal frequency to a baseband of 10 kHz width. The system is laid out for two frequencies at 78.9 and 104.02 GHz. Making the measurement at two different frequencies can be helpful in discerning systematic effects in the resulting maps, for instance caused by multiple reflections. The receiver is also tunable around each of these frequencies by 130 MHz for similar reasons. The signal horn is a conical, grooved cylindrical waveguide horn, while the reference horn is of similar design and equipped with a lens to provide a reference beam with a beam width of 4.6 degrees at the half-power points.

As is clear from the theoretical treatment above, it is imperative that we know the amplitude and phase function of both the reference and the signal feed as accurately as possible. The phase function must be subtracted from the measured aperture phase before connecting its phase variations to errors in the reflector profile. The feedhorns have been measured with great care on the indoor range at IRAM in Grenoble (IRAM Internal Report, June 2002, by Lazareff, Carter, Halleguen and Degoud). The results were compared with model calculations using an advanced electro-magnetic simulation package and excellent agreement was found. The phase pattern of the feeds have an estimated error of less than one degree, while the amplitude taper at the edge of the reflector aperture is -6 dB. This is more than we would like (a free–space taper of 2.5 dB has to be added to the measured level) for a high signal to noise ratio in the outer part of the reflector; an actual level of -6 dB is preferred. For the measurement of the 64 ALMA production antennas this feed should be replaced by one which provides such a taper.

6.3.2 Backend

The backend of the receiver is essentially a digital signal processor (DSP) where the narrow-band signals are digitized and correlated. Both the "sine" and "cosine" part of the complex correlation function are obtained, which are then transformed to the amplitude and phase functions.

6.3.3 Transmitter

The transmitter consists of a single photo-diode, directly coupled to a waveguide horn, which is fed through an optical fiber by two optical signals at different frequencies near a wavelength of ~ 1550 nm. The photo-diode provides a mixing signal at the difference of the two optical signals, tunable roughly from 78.7 to 79.0 GHz (low band) and 103.8 to 104.2 GHz (high band), with an output power of about 10 nW, leading to an EIRP of about 20 W. The transmitter is placed on top of a 50 m high tower at a distance of 300 to 325 m from the aperture of three antennas at the site, resulting in a measurement elevation angle of about 9 degrees.

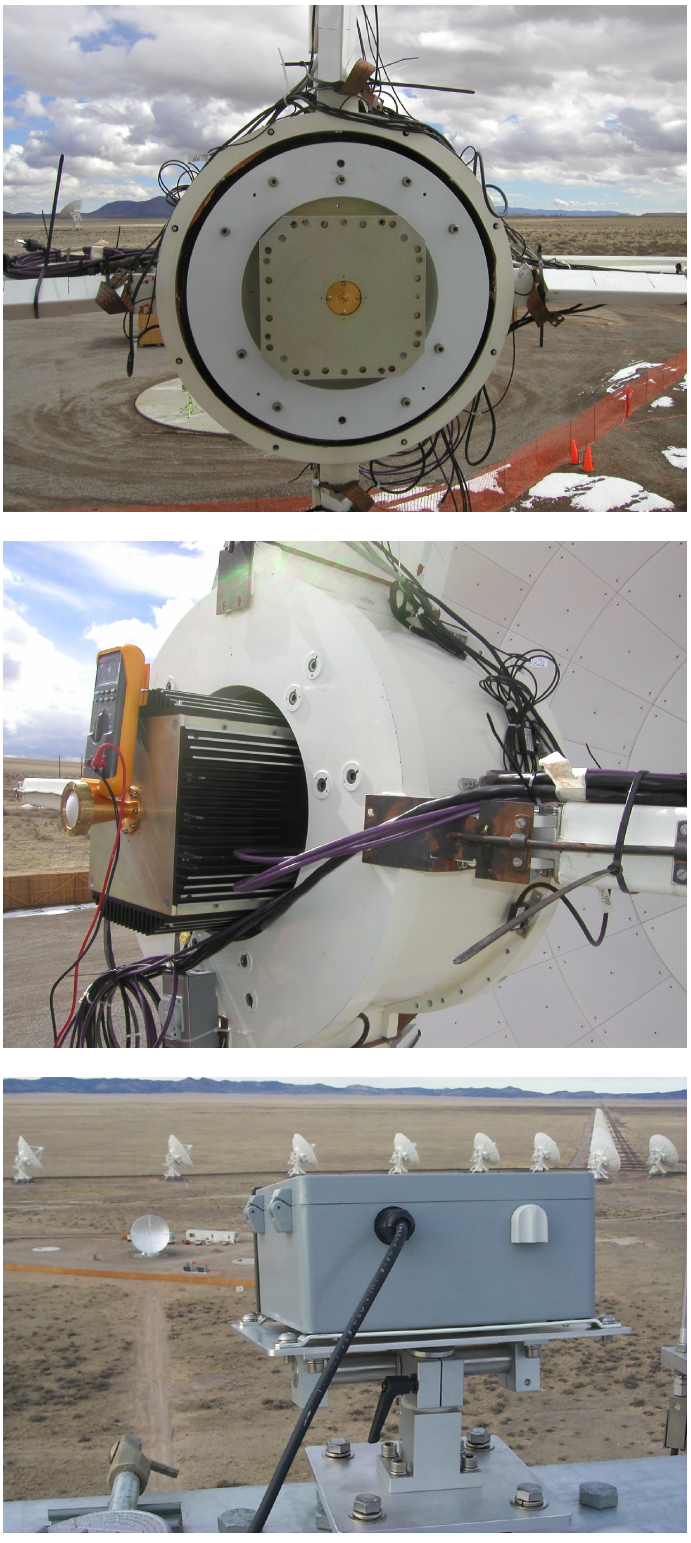

Figure 8: Holography system hardware. Signal feed side of the frontend (top); reference feed side of the frontend (middle); and transmitter.

7 Holographic Data Acquisition

To derive typical values for the various holography map parameters, map parameters, we set the following boundary conditions:

1. The data rate is the canonical 12 msec per sample, which means about 80 samples per second.
2. The fine tuning feature of the holography receiver allows for the search for ground reflection.
3. A goal for the total time for one map is less than one hour.
4. The required aperature plane resolution is $\leq$ 20 cm. This yields $\geq$ 25 independent points per square meter of reflector surface.
5. Oversample by a factor of at least 2 to minimize aliasing.

Based on the equations listed in Appendix A and taking

$$\begin{aligned} f_1 &= 1.13(6 + 2.5 \text{ dB taper}), \\ \nu &= 78.92 \text{ and } 104.02 \text{ GHz}, \\ \theta_b &= 74'' \text{ and } 56'', \end{aligned}$$

we obtain the typical holography map parameters of Table 3.

Table 3: Typical Holography Map Parameters

Map Type	δ_d (cm)	f_{osr}	θ_{ext} (deg)	θ_{sr} ($''$)	$\dot{\theta}$ ($''$/sec)	N_{row}	f_{oss}	t_{map} (hr)
Standard	20	2.2	1.64/1.24	33/25	300	180	20/15	0.96/0.73
Fine	13	2.2	2.46/1.87	33/25	600	270	40/30	1.08/0.82
Less OS	20	1.4	1.64/1.24	53/40	300	112	20/15	0.61/0.46

Assumes constant $f_1 = 1.13$ (6 + 2.5 dB taper).

Assumes $\nu = 78.92/104.02$ GHz and $\theta_b = 74/56$ $''$.

Assumes apodization smoothing factor $f_{apo} = 1.3$.

8 Holographic Data Analysis

8.1 Description

Data analysis uses the CLIC data reduction software of the Plateau de Bure interferometer. The raw data, written by the on-line software in the ALMATI-FITS data format (Lucas *et al.* , 2001), is converted to Plateau de Bure format using **CLIC**.

The data are then calibrated and imaged using **CLIC**. The two main operations are:

1. *Calibrate data in amplitude and phase*, based on bore-sight measurements at beginning and end of each map row, assuming gradual drift in amplitude and phase with time. This uses the standard amplitude and phase calibration commands: `SOLVE PHASE, STORE PHASE, SOLVE AMPLITUDE, STORE AMPLITUDE`.

2. *Compute the aperture map and fit panel displacements and deformations*: This is implemented in command `SOLVE HOLOGRAPHY`. The mathematics are in §5.

   The data processing steps are:

   (a) *Interpolate data to a regular grid* in antenna-based coordinate system. This grid matches the observed system of rows (same number and separation). This grid is further extended, by addition of zeroes, to a user-specified size, in order to get a finer interpolation of the output aperture map: 64x64, 128x128, 256x256 and 512x512 sizes are available.

   (b) *FFT to aperture plane.* This is replaced by a more complex transformation if one takes into account the first non-Fresnel terms. This is described in §5.

   (c) *Compute phases in the aperture plane.*

   (d) *Apply the geometrical phase correction*: this is

   $$\Delta p = \frac{\rho^2}{2R} - \frac{\rho^4}{8R^3} + \sqrt{\rho^2 + (f + \delta f - \frac{\rho^2}{4f})^2} - (f + \frac{\rho^2}{4f} + \delta f)$$

   where ρ is the radius in the aperture, f the focal length of the primary, δf the refocusing used to compensate for the finite transmitter distance R (δf is the distance between the holographic horn phase center and the antenna prime focus). See §5.

   (e) *Correct for measured feed phase diagram.*

   The measurement is described in the memo by Lazareff *et al.* (2003).

   (f) *Mask edges and blockage.*

   (g) *Fit and remove 6 phase terms:* constant, 2 linear gradients, 3 focus translations. They account for a phase offset, an antenna pointing error (constant during the measurement) and a small displacement of the holography horn relative to the nominal focus position ($f + \delta f$ above). One may keep fixed either the X and Y coordinates or all three X, Y, Z coordinates.

   (h) *Convert to normal displacement map.*

   (i) *Plot amplitude and phase maps.*

   (j) *Fit panel displacements (optionally deformations) and screw adjustments.*

   In CLIC we deconvolve for finite resolution effects by an iterative procedure (subtracting the truncated field of the fitted panels from the measurements, to get the next order correction, ...). The screw settings are output in a text file (*e.g.* `23-jul-1996-Vertex.panels`).

We introduced also a correction to add empirically an offset to the central pixel of the beam map, in order to partially cancel the ring pattern. The best offset was selected on the basis of the improvement on the final surface rms. This did not prove very successful in removing the ringing pattern.

8.2 Using the GUI Interface

- Type `clic` in a terminal window.
- Type `@ ATFdefine`. A small menu window should appear on the screen.

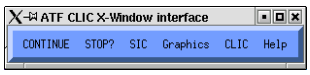

- In menu `CLIC`, select `ATF Holography reduction`. This causes a graphic window to appear, as well as a dialogue window.

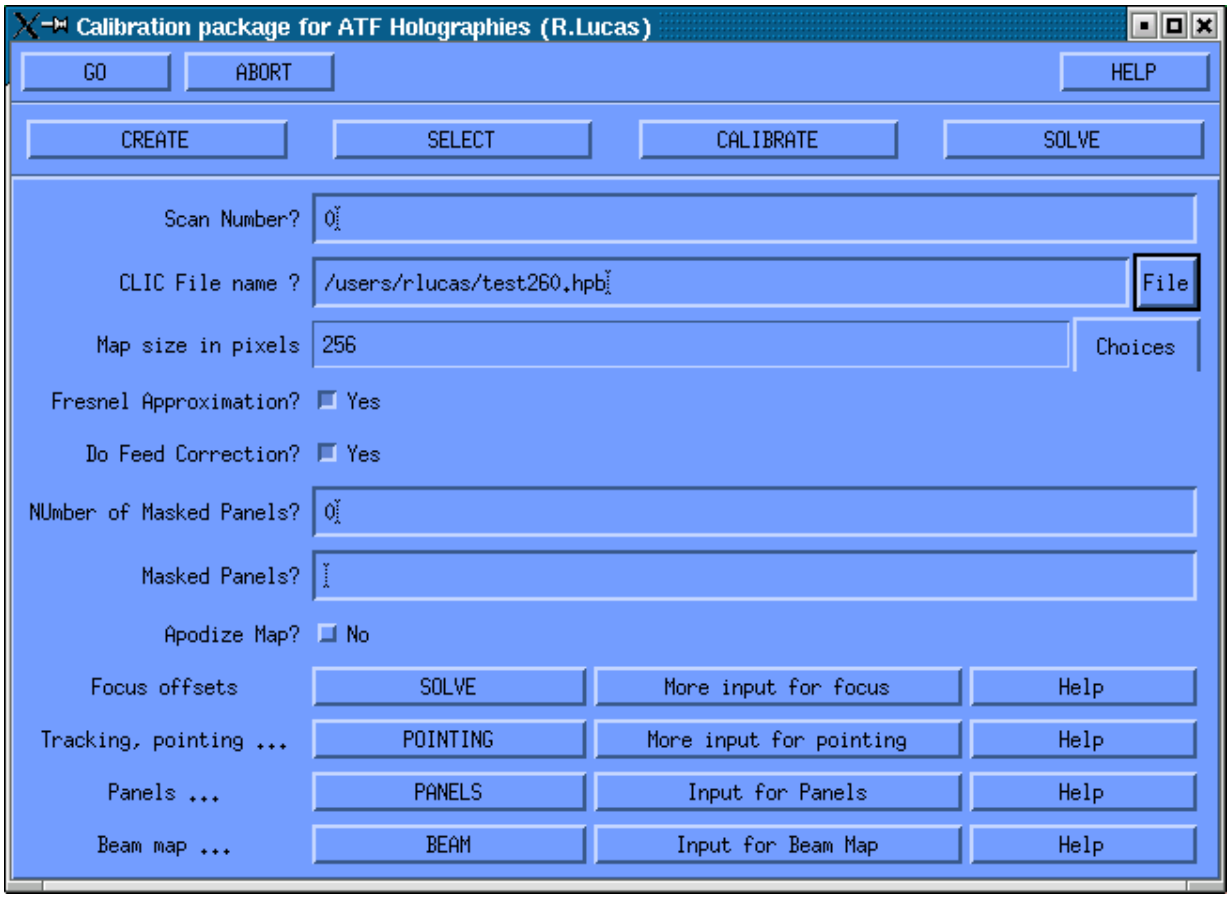

- Enter the scan number (there is one FITS file per scan; they reside in `/users/oper/HOLODATA/` under the names `TESTnnnn.FITS`, where `nnnn` is the scan number).
- Press "`CREATE`". This will copy the FITS data into a CLIC data file. Its name will be `testnnnn.hpb`.
- Press "`SELECT`". You should get a plot of angular offsets versus scan number.

- Press "`CALIBRATE`". Amplitude and phase of the boresight measurements will be displayed together with a red curve fit. Enter `continue` or press `CONTINUE` at the left of the ATF menu window, if the fit looks all right, in order to store it within the data headers.

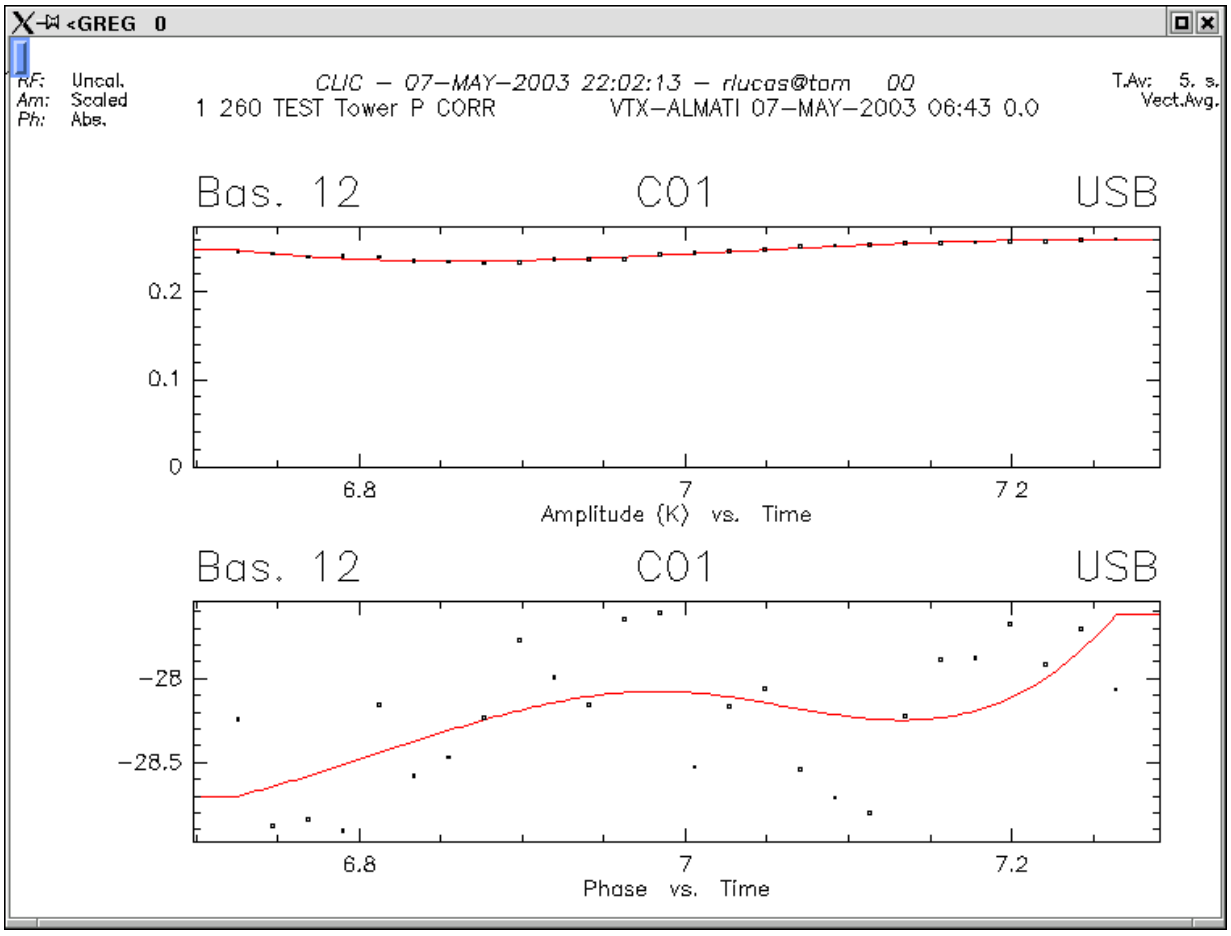

It the fit fails, e.g. due to fast variations, or bad points :

  - You may change the step of the spline fuction (`SET STEP value`, with value in hours), then `SOLVE AMPLITUDE PHASE /PLOT`, to get a new fit.
  - Or you may delete a bad point by finding its observation number:
    * enter `CURSOR`, point with the mouse to the bad point and type '`H`'. The first number listed will be the observation number `n` .
    * Then type `DROP n` to eliminate this observation from the current index.
    * Then type `SOLVE AMPLITUDE PHASE /PLOT`, to get a new fit.
  - When you are satisfied, do not forget to type `C` (for `CONTINUE`), so that the calibration is stored within the data headers.

- Select the map size in pixels (64 to 512). It should be higher than the actual number of rows in the observed beam map, (or information will be lost).

- Press "SOLVE". The map should appear in the graphic window.

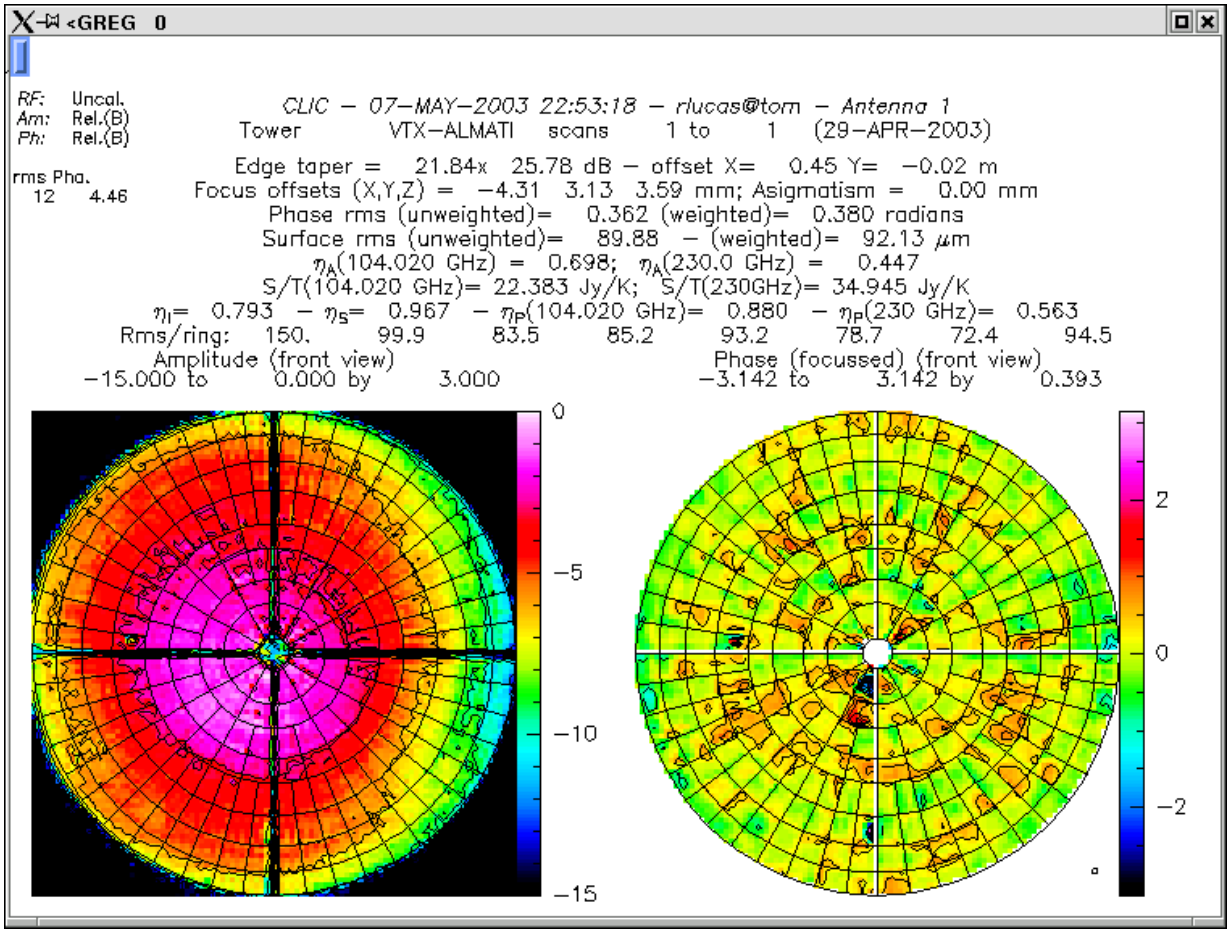

The map header contains, among other parameters:

  - the illumination parameters,
  - the phase rms (unweighted and weighted by the amplitude),
  - the surface rms (also weighted and unweighted),
  - aperture efficiencies (calculated using the observed illumination and the geometrical blockage, for the observed frequency and 230GHz), and the corresponding Jy to Kelvin conversion factors,
  - illumination efficiency, spillover efficiency, and phase efficiencies (Ruze factors)
  - the surface rms in each ring.

- Additional parameters in the main window:

  - *Fresnel Approximation*: when selected, the additional terms (see §4.
  - *Do feed Correction*: to be unselected for testing only.
  - *Number of masked panels*: the number of panels to be ignored for the fit and the calculation of RMS surface errors. Their numbers are entered in the box below. The panel numbering scheme is in Appendix C.

– *Apodize Map*: to apodize the observed map in order to reduce/suppress the 'ringing' along the quadrupod legs and map edges. The weighting function is a cosine reaching zero at the map edges.

- Additional input windows (to call them press on e.g. "`More input for focus`", and the similar boxes below):

  – `Focus offsets`: Enter here the focus offsets in mm. The corresponding corrections are applied to the phase map before fitting for focus displacements. This enables overcoming the 2π discontinuities in the phase map. One may also fix either the X and Y focus coordinates, or all X, Y and Z to these values.

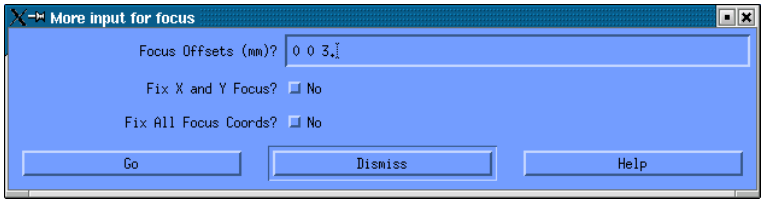

  – `Tracking, Pointing` : The input map can be displaced to compensate for pointing errors, if they are larger than a fraction of a beam. Naturally it is preferred to peak up on the transmitter before taking the map. One may also enter a 'fudge factor' to correct for a tracking error which changes sign between odd and even rows of the map.

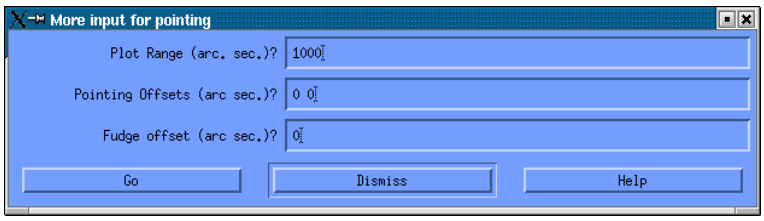

  – The last row is used to `plot a beam map`.

- To obtain the list of screw settings: Press "`PANELS`". A file such as `23-nov-2001-Vertex.panels` is created (where positive numbers mean that the panels should move towards the subreflector). It contains the screw motions in micrometers. At the end of the calculation the left part of the screen displays the fitted panel shapes, while the right one displays the fit residuals.

- Specific options for this last step can be seen and entered by pressing "`input for panels`". Additional input include:

  – *Modes:* the fitted degrees of freedom for panel fitting; the last two actually deform the panels:

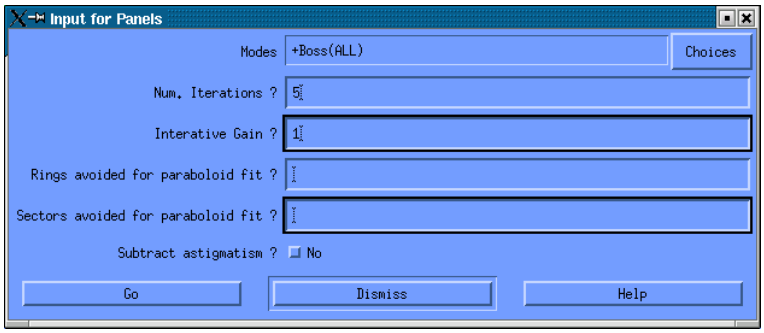

Piston only 1 translation mode (normal to antenna surface)

+Tilts 3 modes: panel tilts around two perpendicular axes in the tangent plane to the paraboloid are added

+Torsion 4 modes: a panel torsion is added

+Boss 5 modes: the motion of panel center relative to the edges is added.

– *Number of iterations:* usually 5 is OK

– *Iterative gain:* usually 1 works

– *Rings avoided for paraboloid fit:* One may take out specific rings of the paraboloid fit (e.g. to adjust one or several ring relative to the others).

– *Sectors avoided for paraboloid fit:* One may take out specific sectors of the paraboloid fit (e.g. to adjust one sector relative to the others).

– *Substract astigmatism:* Take out the astigmatism component before fitting the panels.

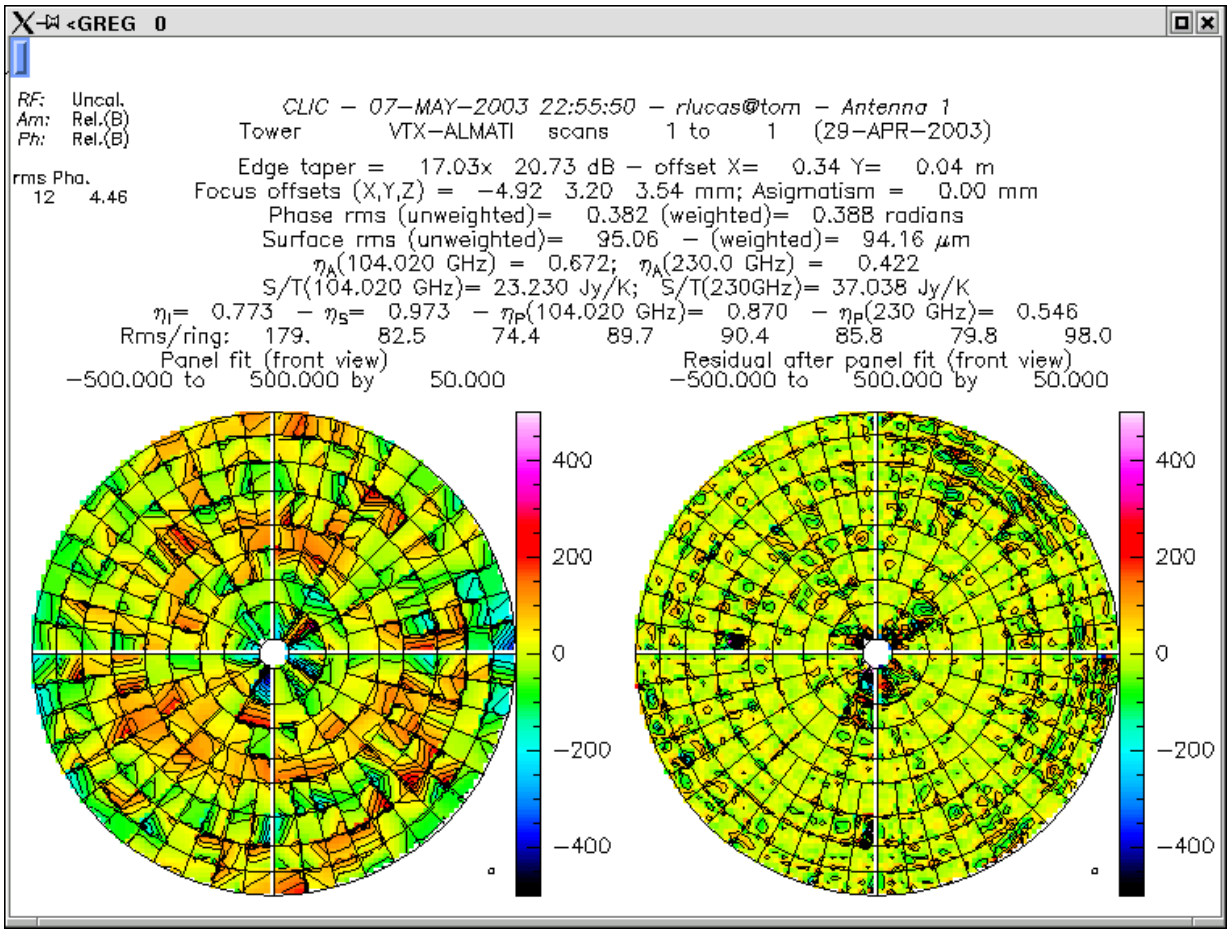

- Sample screw listing (Positive screw settings mean that the panel has to move closer to the primary focus, or "up"):

```
 Output from CLIC\SOLVE HOLO            3
 CLIC - 07-MAY-2003 22:55:50 - rlucas@tom - Antenna 1
 Tower        VTX-ALMATI   scans     1 to     1   (29-APR-2003)

Panel ring n0.  1:
 Sec/Pan     Screw settings (1-5), [mum]
    1-11       -192( 37)  -216( 37)   -36( 59)  -117( 59)  -117( 28)
    2-11        -36( 41)   105( 41)  -167( 64)   319( 64)   -11( 31)
    3-11       -230( 30)  -174( 30)   -79( 48)   115( 47)  -100( 22)
    4-11        -97( 28)  -107( 28)   -42( 44)   -78( 44)   -72( 21)
    5-11        -82( 29)  -127( 29)    -3( 44)  -156( 44)   -68( 21)
    6-11       -174( 33)  -165( 33)    30( 52)    59( 52)   -47( 25)
    7-11       -159( 15)  -229( 15)   127( 23)  -116( 23)   -41( 11)
    8-11        -38( 22)   -32( 22)    77( 34)    97( 34)    34( 16)
    9-11       -499( 61)  -469( 61)  -197( 96)   -92( 96)  -298( 46)
   10-11        -39( 49)   -16( 49)   -59( 79)    20( 78)   -34( 37)
   11-11          5( 29)   -81( 29)   115( 45)  -181( 45)     8( 21)
   12-11       -161( 23)  -267( 23)   113( 37)  -251( 37)   -76( 18)
```

Panel ring n0. 2:

Sec/Pan	Screw settings (1-5), [mum]				
1-21	9(19)	86(19)	-100(19)	7(19)	-11(9)
2-21	-67(32)	18(32)	-182(31)	-65(31)	-87(16)
3-21	-2(12)	-70(12)	-21(12)	-115(12)	-44(6)
4-21	-20(23)	-11(23)	-48(23)	-35(23)	-30(11)
5-21	-30(18)	-77(18)	52(17)	-13(17)	-10(9)
6-21	-3(9)	-35(9)	66(9)	21(9)	18(4)
7-21	59(18)	-31(18)	80(18)	-44(18)	27(9)
8-21	-30(13)	50(13)	-45(13)	66(13)	0(7)
9-21	57(38)	58(38)	175(39)	176(38)	119(19)
10-21	-39(15)	-19(15)	27(15)	55(15)	5(8)
11-21	-42(11)	-101(11)	0(11)	-82(11)	-48(6)
12-21	-60(13)	-72(13)	-16(13)	-32(13)	-43(6)

Panel ring n0. 3:

Sec/Pan	Screw settings (1-5), [mum]				
1-31	-33(13)	-13(13)	13(14)	44(13)	4(6)
1-32	35(13)	-6(13)	98(14)	37(14)	43(6)
2-31	30(11)	-42(11)	41(11)	-65(11)	-9(5)
2-32	-130(24)	-100(24)	81(26)	125(25)	0(10)
3-31	-90(12)	-19(12)	104(12)	209(12)	57(5)
3-32	-66(20)	-126(20)	192(22)	103(21)	33(9)
4-31	113(13)	-34(13)	108(14)	-110(14)	18(6)
4-32	90(19)	111(19)	12(20)	43(19)	62(8)
5-31	-121(27)	-152(27)	26(29)	-21(29)	-63(12)
5-32	26(23)	46(23)	-84(24)	-55(24)	-20(11)
6-31	141(16)	72(16)	154(16)	52(16)	104(7)
6-32	24(16)	45(16)	-5(17)	25(17)	22(7)
7-31	-47(11)	-110(11)	-9(12)	-101(12)	-66(5)
7-32	12(14)	-2(14)	126(15)	105(15)	63(6)
8-31	89(11)	58(11)	98(11)	52(11)	74(5)
8-32	13(6)	7(6)	50(7)	41(7)	29(3)
9-31	31(20)	16(20)	68(21)	47(21)	42(9)
9-32	-49(22)	-38(22)	-70(24)	-54(23)	-53(10)
10-31	-120(20)	-48(20)	1(21)	107(21)	-11(9)
10-32	26(14)	7(14)	72(15)	44(15)	38(6)
11-31	21(10)	9(10)	154(10)	136(10)	84(5)
11-32	-40(16)	-41(16)	30(17)	29(17)	-3(7)
12-31	38(8)	24(8)	23(8)	3(8)	21(4)
12-32	-126(19)	-40(19)	-53(20)	73(20)	-34(9)

Panel ring n0. 4:

Sec/Pan	Screw settings (1-5), [mum]				
1-41	86(11)	10(11)	152(11)	58(11)	70(5)
1-42	33(12)	7(12)	16(13)	-16(12)	12(6)

```
   2-41        -21( 15)   -76( 15)    12( 16)   -56( 16)   -38(  8)
   2-42        113( 14)    48( 14)   114( 15)    34( 15)    78(  7)
   3-41        156(  9)   135(  9)   111(  9)    85(  9)   127(  4)
   3-42         34( 18)   121( 18)    41( 19)   148( 18)    84(  9)
   4-41        114( 29)   142( 29)    81( 30)   115( 30)   116( 14)
   4-42          7( 20)    55( 20)   -13( 21)    47( 21)    25( 10)
   5-41        -35( 21)    89( 21)   -29( 22)   124( 22)    35( 10)
   5-42         94( 10)    88( 10)    77( 10)    70( 10)    84(  5)
   6-41         73( 17)   109( 17)   -58( 18)   -13( 18)    41(  9)
   6-42         83( 14)    16( 14)   105( 15)    23( 14)    55(  7)
   7-41        -23( 19)    -2( 19)   -36( 20)    -9( 20)   -17(  9)

... and so on until:

  12-84       -231( 46)   -31( 45)  -262( 47)   -41( 46)  -141( 21)
```

9 Holography Measurement Results for the VertexRSI Antenna

The antenna was delivered with a nominal surface error of $\approx 80\mu$m RMS, as determined from the photogrammetric measurement. However, the location of the focal point of the paraboloidal reflector was not determined by this measurement; in other words, the position of the best fit focus was left free.

Our first holography map showed an RMS of $\approx 85\mu$m. However, the focal point was displaced sideways from the axis by more than 5 mm. We decided to bring the focus on-axis; the resulting rms increased to $\approx 150\mu$m. A first setting of the surface resulted in an RMS of 64μm. In four more steps of adjustment the surface error decreased to 19μm RMS.

The sequence of surface error maps, along with the RMS and the error distribution is shown in Figure 9. As allowed in the specification, we have applied a weighting over the aperture proportional to the illumination pattern of the feed. This essentially diminishes the influence of the surface errors in the outer areas of the reflector. To illustrate the difference this makes, both the weighted and unweighted RMS values are plotted in the graphs of Figures 13 and 13. The white areas in the surface error maps are bad panels, which could not be set accurately. They were left out of the calculation of the final overall rms value.

With increasing accuracy the presence of an artefact in the outer area of the aperture became apparent. There is a "wavy" structure in the outer section with a "period" too large to be inherent in the panel. The structure is clearly visible in Figure 9 and its period is not related to the size of the panels. Thus it is unlikely to be caused by systematic effects in the panels or their adjustment on the backup structure. Experiments with absorbing material showed that it was not caused by multiple reflections. The effect can be described

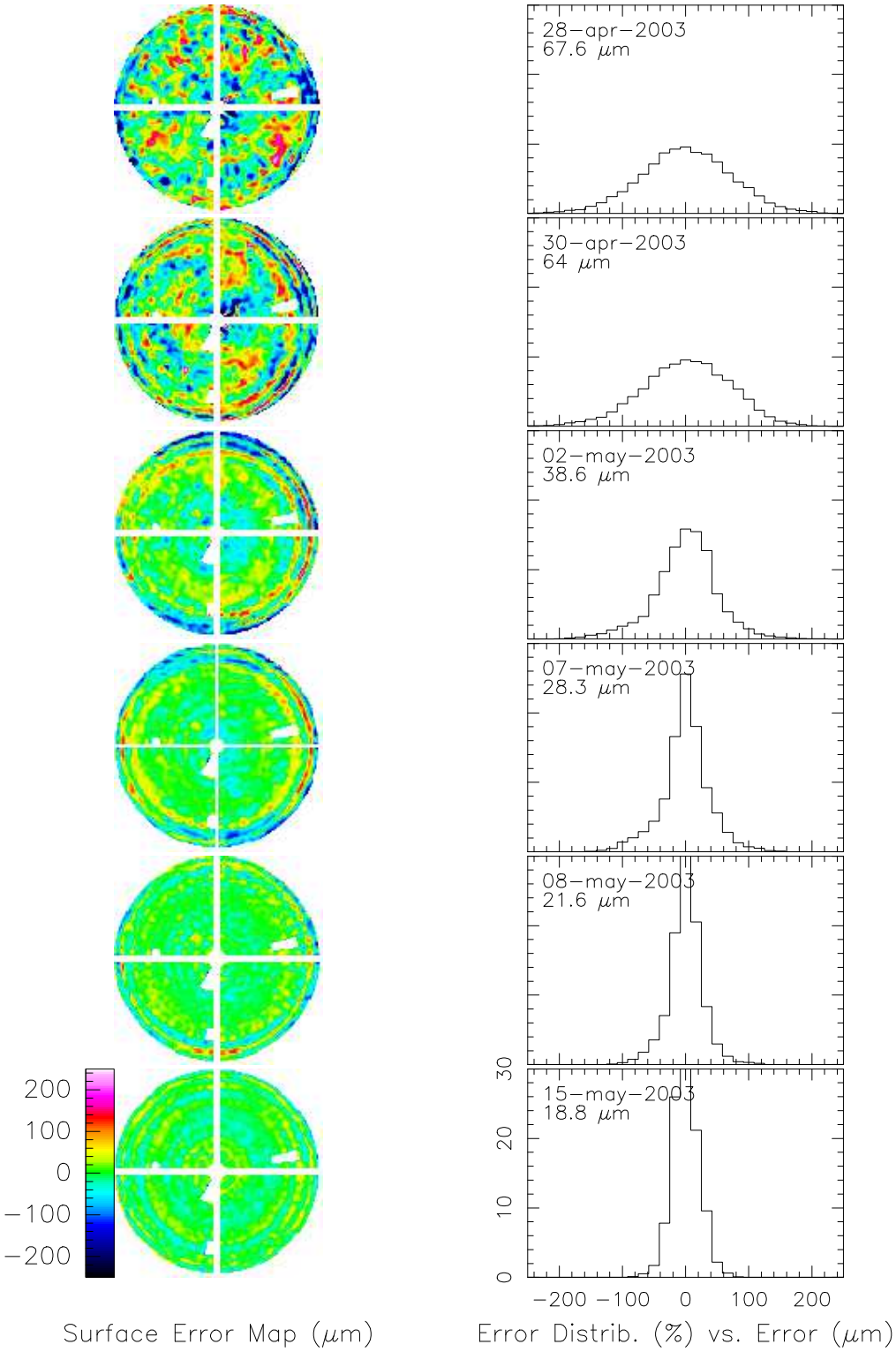

Figure 9: Sequence of surface error maps with intermediate panel setting. The surface contours are shown on the left side; the error distribution on the right. The white cross and the small white areas represent the quadripod and a few faulty panels and were not considered in the calculation of the rms error.

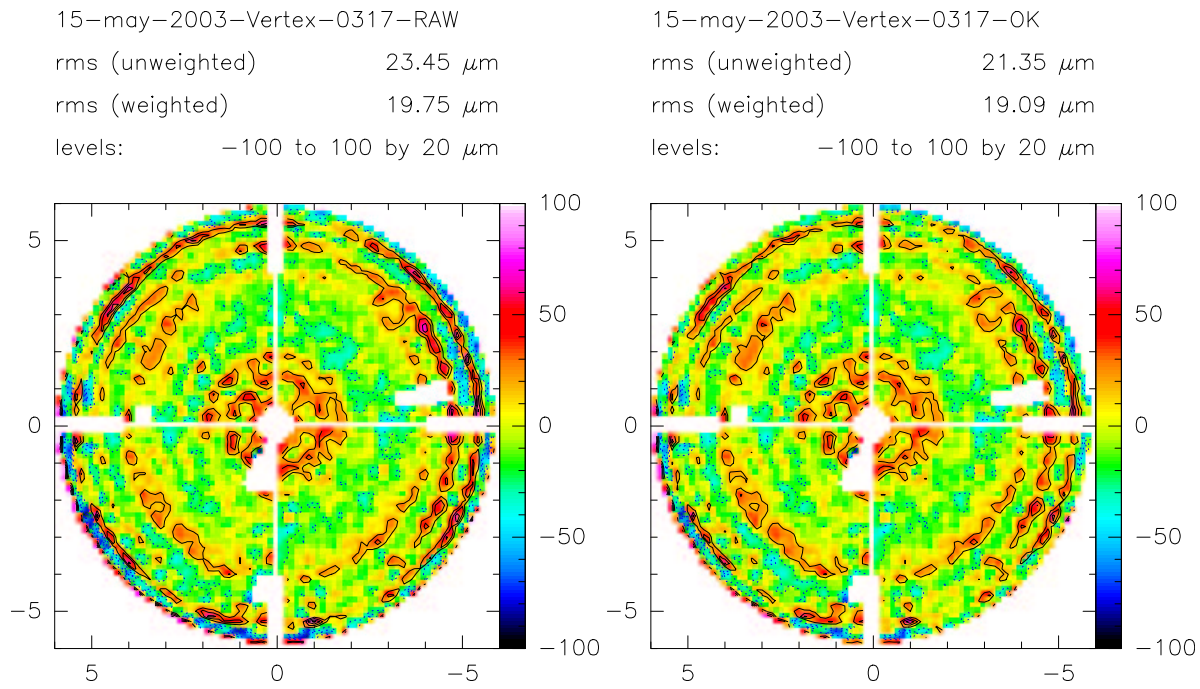

Figure 10: The map on the left is the result of the measurement, showing the "waviness" in the contours in the outer part of the reflector. In the right hand map the data have been manipulated to decrease the effect of the waviness. Some improvement is visible. On the whole the effect appears to have only a small influence on the derived rms error.

by a DC-offset in the central point of the measured antenna map, i.e. some saturation on the point with the highest intensity. By adjusting this offset in the software, most of the artefact could be removed. This is shown in Figure 10, where this procedure has been applied to the data of the left panel and the result is shown on the right. Some improvement in the outer area of the map is visible, although the improvement in the overall RMS error is not large. We have applied such a correction to the data of the final maps. We return to this point in the concluding discussion.

The adjustments were done with a simple tool. Two people on a man-lift approached the surface from the front, where the adjustment screws are located (see Figure 11). The time needed for an adjustment of the total of 1320 adjusters was 8 hours. The specification requires a full adjustment in 8 hours. In the series production, with the use of a more automated tool, this should be readily achievable.

The best surface maps were obtained at night. They consistently show an RMS of about 20μm. To estimate the accuracy and repeatability of the measurements, we produced difference maps between successive measurements throughout the measurement period. The rms difference between consecutive maps is normally less than 10μm, typically 8μm. An example of a difference map is shown in Figure 12. The map of measurement number 307 is shown on the left, while the right hand side shows the difference between map 307 and 308, made about one hour later. Daytime maps tend to be somewhat worse, typical values of the RMS lie between 20 and 25μm. Part of this is certainly due to the atmosphere, even over the short path length of 315 m.

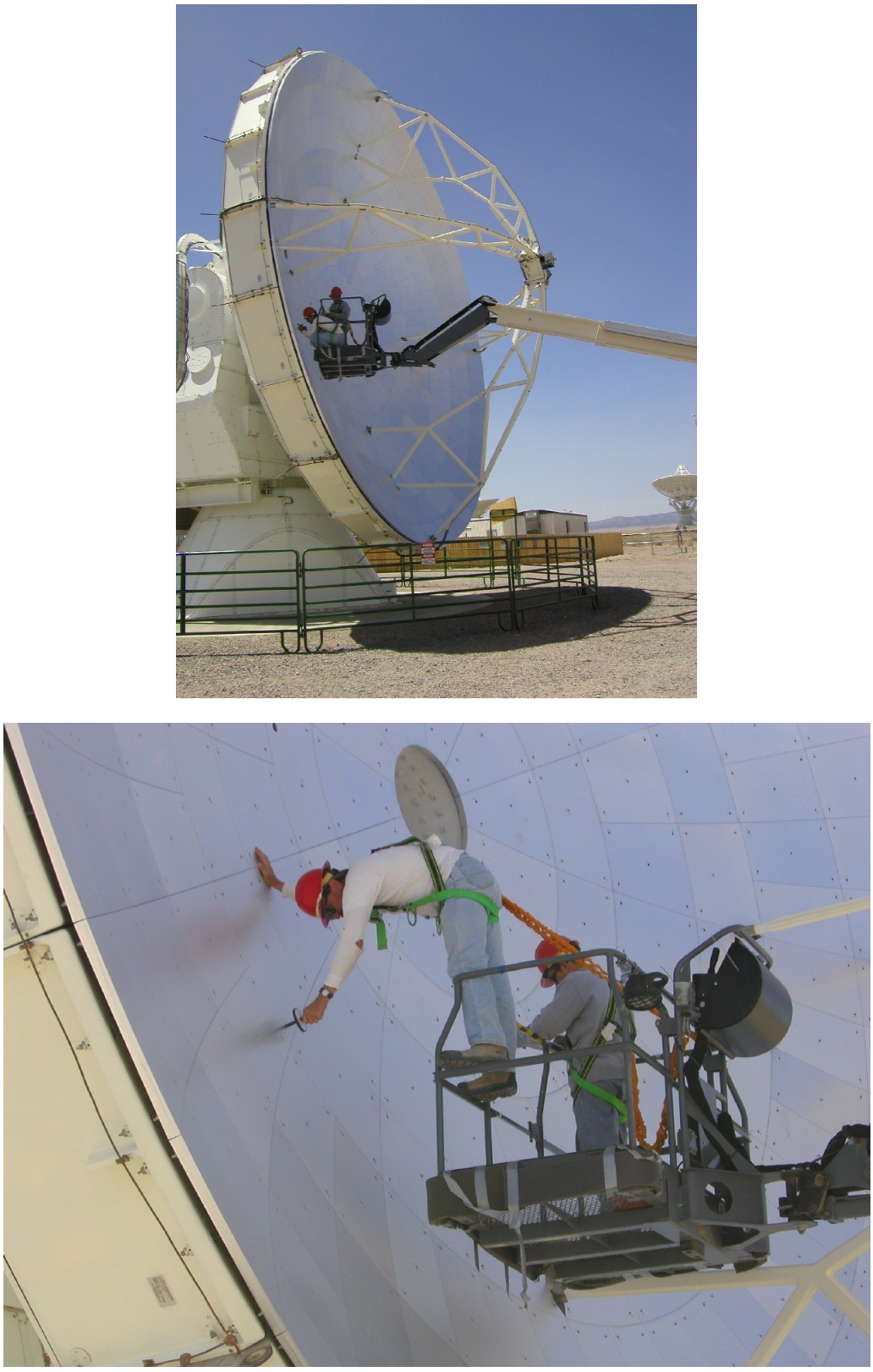

Figure 11: Panel adjustment of the VertexRSI prototype antenna.

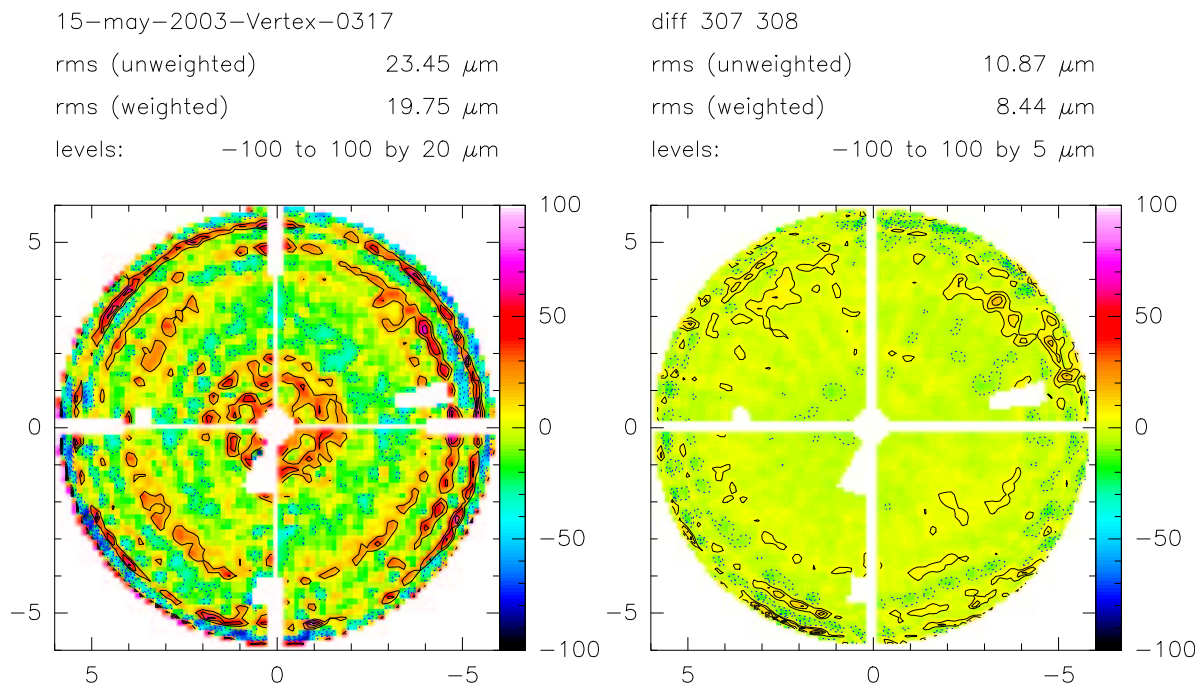

Figure 12: Example of the repeatability of the measurements. The map on the right is the difference between the one at left and a map made one hour afterwards. The RMS of the difference maps is about 8μm, which is commensurate with the expected value due to noise and atmospheric fluctuations.

We have made series of maps while changing the orientation of the antenna with respect to the Sun. Also maps were made under quite different wind conditions. The resulting rms values are all very close. In Figure 13 we show the derived RMS of 11 maps, made on 13-14 May 2003, along with the variation of environmental conditions during the measurements. Obviously these effects have at worse only a small influence on the surface error. A similar behaviour was found in a series of 32 maps, made in five consecutive days, 13-18 June 2003, as shown in Figure 14. The increase in the average rms from 20 to 22μm between early May and mid June is almost certainly caused by the deteriorating atmospheric conditions during the Summer at the site, where the humidity has significantly increased.

Note that to increase the RMS from 20 to 22μm, the "additional" component has a magnitude of 9μm RMS! It can be stated that the measured small differences are fully consistent with the expected contributions from temperature changes and wind forces, as allowed by the specification (panel: 4μm each for wind and temperature, BUS: 5μm for wind and 7μm for temperature). Actually, the measured differences can also be explained on the basis of the accuracy of the holography measurement alone.

Barring undetected systematic errors (see the discussion in §6), we estimate the overall error in the final averaged surface maps to be about 5μm RMS.

From the holographic measurement of the VertexRSI antenna we reach the following conclusions:

1. The holography system has functioned according to specification and has enabled us to measure the surface of the antenna reflector with a repeatability of better than

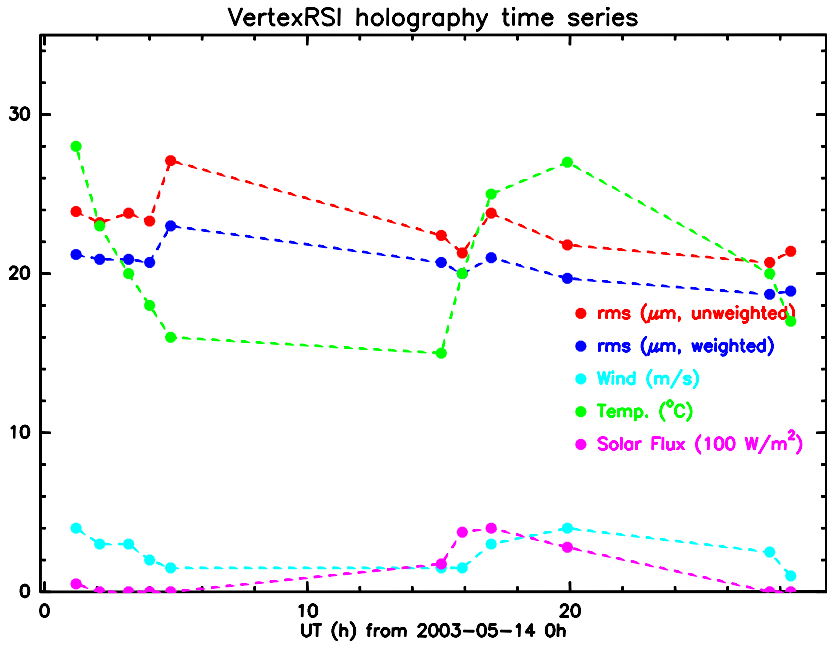

Figure 13: Time series of the holography of the VertexRSI antenna over a period of two days in May 2003. The weighted (applying the illumination function, taper) and unweighted RMS values are given along with temperature, wind speed and solar flux. There is no discernible influence of the varying environmental parameters on the RMS values.

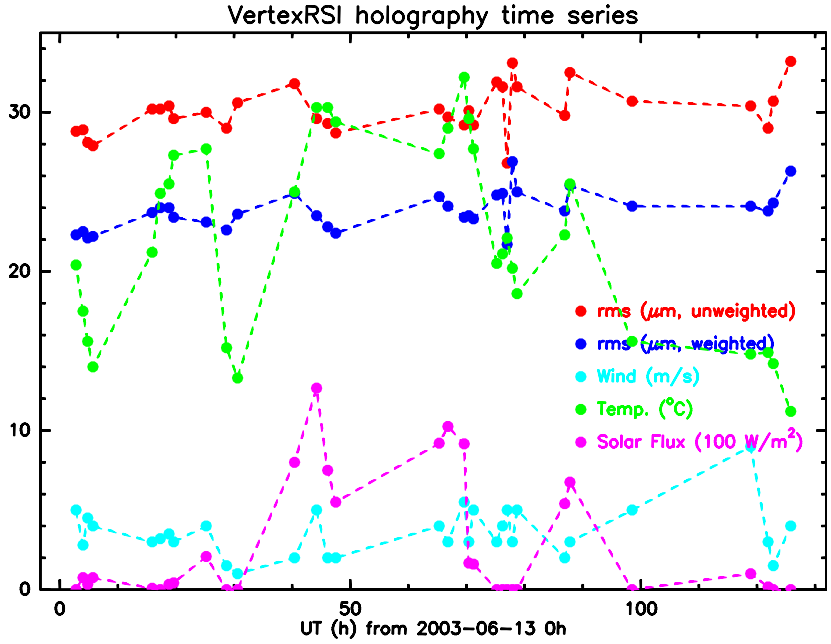

Figure 14: Similar time series as in Figure 13 for the period 13 - 18 June 2003. The slightly poorer surface accuracy measured in June is a reflection of the deteriorating weather conditions (*i.e.* high humidity).

10μm.

2. On the VertexRSI antenna we have achieved a surface accuracy of 19μm RMS after five full and two partial panel settings.

3. With a somewhat more advanced tool than the one used by us, the setting of all 1320 adjusters of the Vertex antenna surface can be accomplished within the specified 8 hours by a team of two people.

4. The small differences in the surface maps obtained over several days of measurement are consistent with the measurement repeatability and at best marginally significant. If taken at face value, they indicate that the deformations of the reflector under varying wind and temperature influence are fully consistent with, and probably well within, the specification.

5. The VertexRSI reflector contains a small number of faulty panels. Two appear mechanically "warped" and could not be brought within specification by adjustment. A few others appear to have a "loose" adjuster(s); no change in shape could be measured despite a significant change in adjustment position. They have been identified and reported to the NRAO antenna group.

6. We have not fully accounted for the cause of the artefact in the outer region of the derived surface maps. We are confident that they do not represent real deformations of the panels in the two outer rings. To fully test the validity of our current ideas as to the reason for this effect, we would need to run an extensive dedicated experiment of an estimated duration of several weeks with participation of the receiver engineers. The available time for the antenna evaluation has not allowed us to do this.

10 Holography Measurement Results for the AEC Antenna

The apex structure of the AEC antenna does not enable us to mount the holography receiver inside the cylinder, as in the case of the VertexRSI antenna. Thus in this case the receiver was bolted to the flange on the "outside" of the apex-structure. Consequently, the feedhorn was brought to the required position by a piece of waveguide of about 500 mm length. This caused significant attenuation in the received signal from the reflector to the mixer. Considering the available transmitter power, we concluded that this would not jeopardise our measurement accuracy significantly. Indeed, as we shall show below, there was no evidence of any negative impact by this receiver and feed arrangement.

The AEC antenna surface was set by the contractor with the aid of a Leica laser-tracker. The RMS of the surface was reported by the contractor to be 38μm. After this measurement an incident caused the elevation structure to run onto the hard stops at high speed. The contractor decided to repeat the surface measurement and obtained an rms of 50μm with some visible "astigmatism" in the surface.

Our first holography map indicated an rms of 55μm with a clearly visible astigmatism. We could identify the high and low regions with those on the final AEC measurement. With two complete adjustments we surpassed the goal of 20μm. A third partial adjustment improved the surface rms to about 14μm . There is no indication of the "artefact" seen in the VertexRSI antenna. We mention the probable reason for this in the conclusion. There is one panel with a large deviation over part of the area. This is believed to have been caused during the measurement and setting procedure by the contractor. We have not included this panel in the computation of the final RMS value. The results of the consecutive adjustments are summarised in Figure 15.

The adjustments were done with a tool provided by the contractor. It was similar to the one used by us on the Vertex antenna, but it was calibrated in "turns" rather than in micrometres. This should be corrected in a possible series production. Again two people on a manlift approached the surface from the front, where the adjustment screws are located. The time needed for an adjustment of the total of 600 adjusters was 7 and 6.25 hours, respectively. The specification requires a full adjustment in 8 hours. Thus this specification is easily met.

From the difference maps we derive a repeatability of about 5μm. An example of a difference map is shown in Figure 16. The differences between maps made under different circumstances are again consistent with the allowed errors due to temperature changes and wind forces and actually of the same order as the estimated measurement accuracy.

Also in this case we made a long series of maps towards the end of the session covering all daily occurring environmental changes. The time series of these measurements are summarised in Figure 17, together with the environmental parameters. The variation in the rms is very small and obviously the influence of the varying temperature and wind effects is small.

On close inspection of the left panel in Figure 16 we see a small "saddle-like" deformation feature in most of the individual panels of the third ring in the form of the reddish islands in Figure 16, left side, middle ring. This has also been seen in other maps. We suggest the following possible reasons for this phenomenon without being able to decide in favour of any of them.

1. If the panels would be slightly warped upon release from the mold, the forces applied to the panel at the five adjusters to "bend" the panel in a best-fitting shape could lead to the observed deformation. Presumably, this effect could be studied by detailed calculations of the stiffness of the panel.

2. A phase error of similar shape can be created by a panel with a focal length different form the specified one. This could be checked by careful measurement of the molds used for the fabrication of the panels. We could radiometrically determine the true focal length of the reflector, and compare that with the theoretical design value, assuming there are no other effects influencing the focal length, like for instance temperature changes.

3. The effect could also be caused by local deficiencies in the mold, which would be "copied" into the individual panels. We consider this unlikely, because the effect is

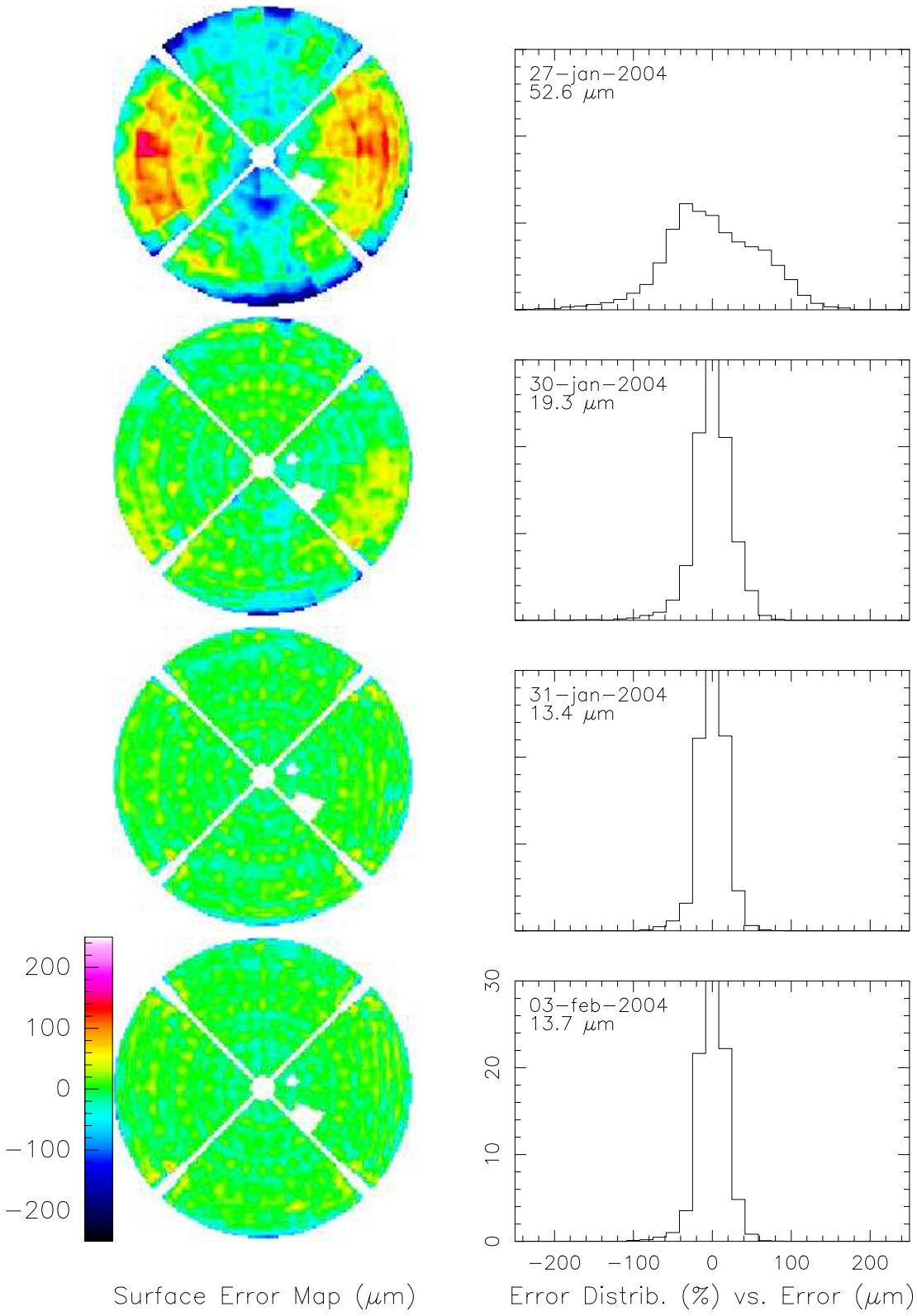

Figure 15: Sequence of surface error maps with intermediate panel setting. The surface contours are shown on the left side; the error distribution on the right. The white cross and the small white area represent the quadripod and a faulty panel and were not considered in the calculation of the rms error.

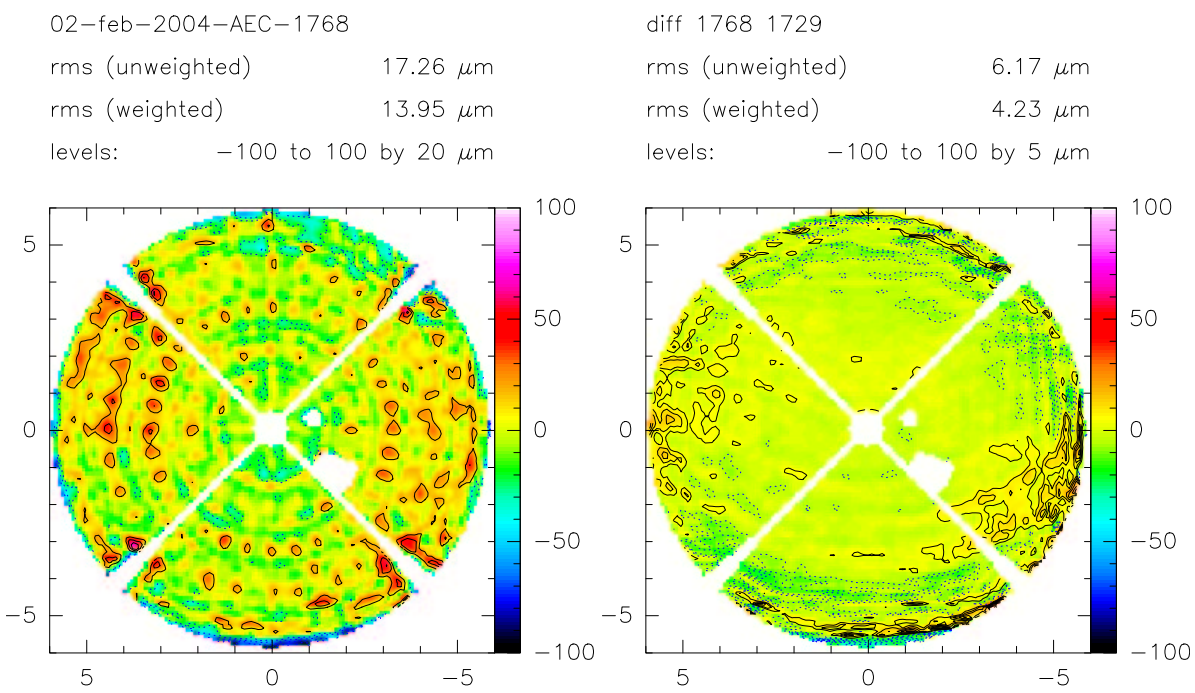

Figure 16: Example of the repeatability of the measurements. The map on the right is the difference between the one at left and a map made one hour afterwards. The rms of the difference maps is about 5μm.

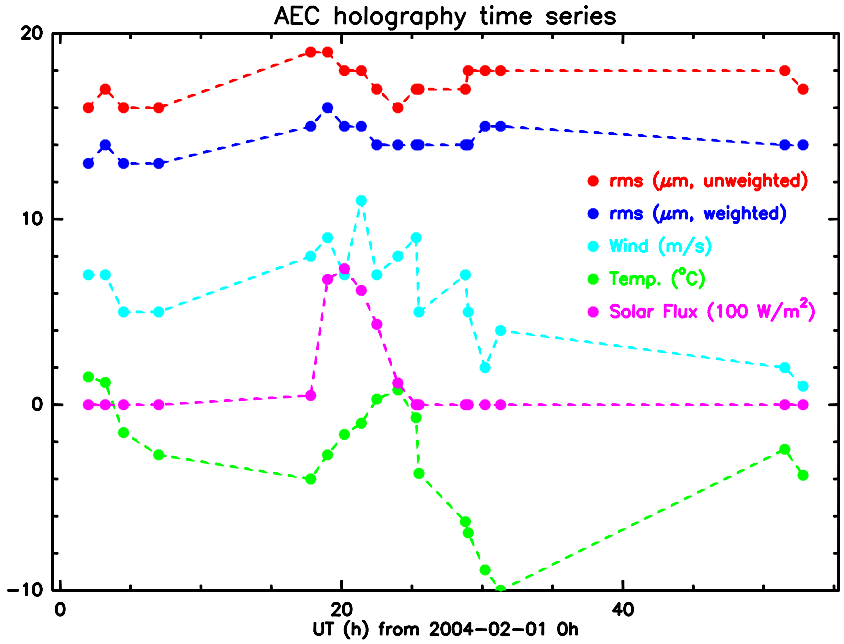

Figure 17: Time series of the holography of the AEC antenna over a period of three days in February 2004. The weighted (applying the illumination function, taper) and unweighted RMS values are given along with temperature, wind speed and solar flux. There is no discernible influence of the varying environmental parameters on the RMS values.

mainly seen in one ring and not all panels in the final map show the effect at equal intensity.

In any case, the effect is small and has not been a hindrance to achieve a very good overall surface accuracy.

From the holographic measurement of the AEC antenna we reach the following conclusions:

1. The holography system has functioned according to specification and has enabled us to measure the surface of the antenna reflector with a repeatability of better than 10μm.

2. On the AEC antenna we have achieved a surface accuracy of 14μm RMS after two full and one partial panel settings.

3. The setting of all 600 adjusters of the AEC antenna surface can be accomplished by a team of two people in less than 7 hours, which is well within the specified 8 hours.

4. The small differences in the surface maps obtained over several days of measurement are consistent with the measurement repeatability and at best marginally significant. If taken at face value, they indicate that the deformations of the reflector under varying wind and temperature influence are fully consistent with, and probably well within, the specification.

5. The AEC reflector contains one faulty panel, strongly deformed in one corner area.

6. We note a small but systematic deformation in the panels of the third ring. We have given some hints as to the possible causes of this effect. Although it does not noticeably deteriorate the overall rms surface error, we suggest that this aspect be studied by the contractor in order to avoid such an effect in possible later deliveries.

11 Concluding Remarks on the Holographic Measurement Activities

We have successfully performed a holographic measurement and consecutive panel setting of the reflectors of the two ALMA prototype antennas to an accuracy of better than 20μm with an estimated measurement accuracy of better than 10μm. The receiver and transmitter system have worked satisfactorily. The data collection and analysis software packages are easy to use and provide quick results of the measurements, directly useable for a panel correction setting. We consider this system suitable for the routine setting of the ALMA production antennas to the goal of 20μm accuracy in an acceptable time span. Modern survey equipment will enable the contractor to deliver the reflector with an accuracy of 50-60 m without undue effort and cost. Although the holography system can easily start with a much larger error, in the former case it is feasible to reach the specification with only one panel setting based on holography.

The longer series of measurements and settings on the Vertex antenna, compared to those on the AEC antenna, are due to the need for us to gain experience with the holography system and analysis and the extra time used for the study of the "ringing" artefact mentioned above. It took us some time to realise that these errors could not be due fully to panel setting deviations. As mentioned earlier, a simple explanation of the observed effect is saturation of the receiver in the central high intensity point of the map. By iteratively adjusting this central intensity level, the ringing effect could be suppressed quite effectively. The fact that the ringing has not been observed with the AEC antenna, where the signal to the receiver is significantly weakened by the long waveguide hints indeed at saturation as the cause for the ringing on the Vertex antenna measurements. A careful determination of the admissible power levels in the receiver would be useful before the system is employed for the setting of the production antennas. We reiterate that through a series of experiments we believe to have shown that the ringing is not due to multiple reflections in the signal path.

In conclusion we can state that the reflectors of both antennas behave equally well. The specification and goal have been met. The variations in surface RMS, measured over time and under changing environmental conditions, are small for both antennas. They are well within the range allowed by the specification and consistent with our measurement accuracy. This excellent behaviour over time is more important than the actually achieved surface setting. We stopped iteration of the settings after having achieved the goal of less than 20mum.

We repeat that these measurements, being performed at one elevation angle only, do not provide information on the gravitationally induced deformation as function of elevation angle. Measurements of these have been performed with the aid of optical instruments and are reported elsewhere in this compendium.

A Some Useful Equations and Calculations

A.1 Definitions

$c \equiv$ speed of light

$\lambda \equiv$ observing wavelength

$f_1 \equiv$ taper factor for signal feed

$f_{apo} \equiv$ apodization smoothing factor

$f_{osr} \equiv$ map oversampling factor between rows

$f_{oss} \equiv$ map oversampling factor along a row

$D \equiv$ main antenna diameter

$d \equiv$ reference feed diameter

$\theta_{ext} \equiv$ angular extent of map (assumed square, in radians)

$\theta_b \equiv$ primary beam size (radians)

$\theta_{sr} \equiv$ sampling interval between rows (radians)

$\theta_{ss} \equiv$ sampling interval along a scan (radians)

$N_{row} \equiv$ number of rows in map

$\delta_d \equiv$ spatial resolution on dish

$\dot{\theta} \equiv$ map row scanning rate

$L_m \equiv$ linear size of map

$P \equiv$ Transmitter EIRP

$P_r \equiv$ Reference feed power received

$P_s \equiv$ Main antenna power received on boresight

$B \equiv$ Detector bandwidth

$t_{int} \equiv$ Integration time

$\alpha \equiv$ Scan angle, which ranges from $-\frac{\theta_{ext}}{2}$ to $+\frac{\theta_{ext}}{2}$

$R \equiv$ Distance between holography transmitter and receiver

$\Delta z \equiv$ Reflector surface displacement accuracy

A.2 Map Resolution and Sampling

$$\begin{aligned} \theta_b &= \frac{f_1 c}{\nu D} \\ &= \frac{61836.6 f_1}{\nu(GHz) D(m)}\ arcsec \end{aligned} \tag{27}$$

$$\begin{aligned} \theta_{sr} &= \frac{\theta_b}{f_{osr}} \\ &= \frac{f_1 c}{f_{osr} \nu D} \\ &= \frac{61836.6 f_1}{f_{osr} \nu(GHz) D(m)}\ arcsec \end{aligned} \tag{28}$$

$$\begin{aligned} \theta_{ss} &= \frac{\theta_b}{f_{oss}} \\ &= \dot{\theta} t_{samp} \\ &= 0.012 \dot{\theta}\ arcsec \end{aligned} \tag{29}$$

$$\begin{aligned} \delta_d &= \frac{D}{N_{row}} \\ &= \frac{f_1 f_{apo} c}{\nu \theta_{ext}} \\ &= \frac{1717.7 f_1 f_{apo}}{\nu(GHz) \theta_{ext}(deg)}\ cm \end{aligned} \tag{30}$$

$$\begin{aligned} t_{map} &= N_{row} t_{row} \\ &= \frac{f_{osr} \theta_{ext}^2}{\dot{\theta} \theta_b} \\ &= \frac{1717.7 \times 10^2 f_{osr} f_1 D(m)}{\dot{\theta}(''/sec) \nu(GHz) \delta_d^2(cm)}\ hours \end{aligned} \tag{31}$$

A.3 Power, Noise, and Sensitivity

$$\begin{aligned} P_r &= \frac{\pi d^2}{4} \frac{P}{4\pi R^2} \\ &= \frac{1}{16} \left(\frac{d}{R} \right)^2 P \end{aligned} \tag{32}$$

$$\begin{aligned} P_s &= \frac{\pi D^2}{4}\frac{P}{4\pi R^2} \\ &= \frac{1}{16}\left(\frac{D}{R}\right)^2 P \end{aligned} \tag{33}$$

$$P_s(\alpha) = P_s(0)\left[\frac{J_1\left(\frac{\pi\alpha D}{\lambda}\right)}{\left(\frac{\pi\alpha D}{2\lambda}\right)}\right]^2 \tag{34}$$

$$\sigma^2 = \frac{\left[kT_{sys}B + P_r + P_s(\alpha)\right]kT_{sys}}{t_{int}} \tag{35}$$

$$\begin{aligned} \delta z &= \frac{\lambda}{16\sqrt{2}}\frac{\sqrt{N_{sx}N_{sy}}}{f_{os}^2}\frac{\sigma_{av}}{M_0} \\ &= 0.044\lambda\frac{\sqrt{N_{sx}N_{sy}}}{f_{os}^2}\frac{\sigma_{av}}{M_0} \end{aligned} \tag{36}$$

For our holography system:

1. $t_{int} = 36$ msec,
2. $M_0 = \sqrt{P_s(0)P_r} = 4.167 \times 10^{-7}$P,
3. $\sigma_0 = (1.23 \times 10^{-22}W(P))^{\frac{1}{2}}$,
4. P_r Term $= (2.13 \times 10^{-27}W(P))^{\frac{1}{2}}$
5. Average map noise for complex correlator $(\sigma_{av}) = (2.23 \times 10^{-25}W(P))^{\frac{1}{2}}$,
6. $\delta z = \frac{1.35\times10^{-2}}{\sqrt{P}}$

Thus, if we want an error in the measurement of the surface shape of $\delta z = 5$ μm, we need a transmitter with an EIRP of P = 7.3 μW. The expected radiated power is in excess of 10μW, so there is a good margin. Noise will not be the limiting factor in the accuracy of the measurement.

B The *Mathematica* Expressions Used to Produce Figures 2 Through 6

Here we present the equations from the main text which have been used to produce the illustrations (Figures 2 through 6) in the *Input* format for the package *Mathematica*.

1. Figure 2 represents Equation 13, which has *Mathematica* form:

$$\lambda = 0.003; k = \frac{2\pi}{\lambda}; R = 300;$$
$$fc = \text{NIntegrate}\left[\text{r BesselJ}[0, ur]\text{Cos}\left[\frac{kr^2}{2R}\right], \{r, 0, 1\}\right];$$
$$fs = \text{NIntegrate}\left[\text{r BesselJ}[0, ur]\text{Sin}\left[\frac{kr^2}{2R}\right], \{r, 0, 1\}\right];$$
$$\text{Plot}[\text{Evaluate}[\{fc, fs, 4(fc^2 + fs^2)\}, \{u, 0, 75\}, \text{PlotStyle} \rightarrow$$
$$\{\{\text{RGBColor}[0,0,1]\}, \{\text{RGBColor}[1,0,0]\}, \{\text{RGBColor}[0,1,0]\}\}, \text{PlotRange} \rightarrow \text{All}]]$$

2. Figure 3 follows from Equation 16 for two different illumination functions (uniform and parabolic):

$$ff = \text{Integrate}\left[r(1 - (1 - t)r^2)\text{BesselJ}[0, ur], \{r, 0, 1\}\right];$$
$$\text{Plot}[\text{Evaluate}[\text{Table}[(4 - 2t)ff, \{t, 0, 1\}], \{u, -10, 10\},$$
$$\text{PlotRange} \rightarrow \text{All}, \text{PlotStyle} \rightarrow \{\{\text{RGBColor}[0,0,1]\}, \{\text{RGBColor}[1,0,0]\}\}]]$$

3. Figure 4 is derived from Equations 23 and 24 and their difference:

$$R = 300; \lambda = 0.003; f = 4.8; \delta f = 0.083;$$
$$pc = \text{Cos}\left[\frac{2\pi}{\lambda}\left(\frac{c^2}{2R} - \frac{c^4}{8R^3}\right)\right];$$
$$fc = \text{Cos}\left[\frac{2\pi}{\lambda}\left(\left(c^2 + \left(f + \delta f - \frac{c^2}{4f}\right)^2\right)^{0.5} - \left(f + \delta f + \frac{c^2}{4f}\right)\right)\right];$$
$$\text{Plot}[\{pc, fc\}, \{c, 0, 6\}, \text{PlotStyle} \rightarrow \{\{\text{RGBColor}[1, 0, 0]\}, \{\text{RGBColor}[0, 0, 1]\}\}]]$$
$$\text{Plot}[pc - fc, \{c, 0, 6\}]$$

4. Figure 5 is also derived from Equations 23 and 24:

$$\text{Clear}[\delta f]; R = 300; f = 4.8;$$
$$p1 = \frac{c^2}{2R} - \frac{c^4}{8R^3};$$
$$p2 = \left(c^2 + \left(f - \frac{c^2}{4f} + \delta f\right)^2\right)^{0.5} - \left(f + \frac{c^2}{4f} + \delta f\right);$$
$$\text{Plot}[\text{Evaluate}[\text{Table}[1000(p1 + p2), \{\delta f, 0.096, 0.106, 0.002\}],$$
$$\{c, 0, 6\}, \text{PlotRange} \rightarrow \text{All}, \text{Frame} \rightarrow \text{True}, \text{GridLines} \rightarrow \text{Automatic},$$
$$\text{FrameLabel} \rightarrow \{\text{Radius in m, Pathlength in mm}\},$$
$$\text{PlotStyle} \rightarrow \{\{\text{RGBColor}[1, 0, 0]\}, \{\text{RGBColor}[0, 1, 0]\}, \{\text{RGBColor}[0, 0, 1]\},$$
$$\{\text{RGBColor}[1, 1, 0]\}, \{\text{RGBColor}[1, 0, 1]\}, \{\text{RGBColor}[0, 1, 1]\}\}]]$$

5. Figure 6 shows the remaining pathlength correction over the aperture from Equation 25. Here the "horizontal" coordinates are the radial coordinates of the aperture and the calculation is made for (u,v)-values at the edge of the beam, as used in the holography measurement (u,v)=(0.03,0.03):

$$R = 300; u = -0.03; v = -0.03;$$
$$\epsilon = \frac{(u\zeta + v\eta)(\xi^2 + \eta^2)}{2R^2} - \frac{(u\xi + v\eta)^2}{2R};$$
$$\text{Plot3D}[1000\epsilon, \{\xi, -6, 6\}, \{\eta, -6, 6\}, \text{PlotRange} \rightarrow \text{All}]$$

C Panel and Screw Numbering System

The same system for numbering the panels and screws were used for both the VertexRSI and AEC antennas. Panels are referenced as `ss-rp`, where:

- `ss` = Sector number, There are as many sectors as panels in inner ring (12).

  They are numbered 01 to 12 starting from right, anti-clockwise, when looking at the primary reflecting surface from the primary focus.

- `r` = ring number, from 1 (inner) to 8 (VertexRSI outer) or 5 (AEC outer).

- `p` = panel position – 1 to 4, anti-clockwise from the same viewpoint, in sector `ss` along ring `r`.

- On each panel, there are five adjusting screws, numbered 1 to 5:

  – 1 and 2 are on the inner side (closest to the center of the dish).

  – 3 and 4 are on the outer side (closest to the edge of the dish).

– 1 and 3 are on the panel left edge when looking from the primary focus, 2 and 4 on the right side.

– 5 is at or near the center of the panel.

Positive screw settings mean that the panel has to move closer to the primary focus ("up").

Figure 18 shows the panel numbering system for the VertexRSI antenna, while Figure 19 shows the panel numbering system for the AEC antenna. Figure 20 shows the screw numbering system for an individual panel on both antennas.

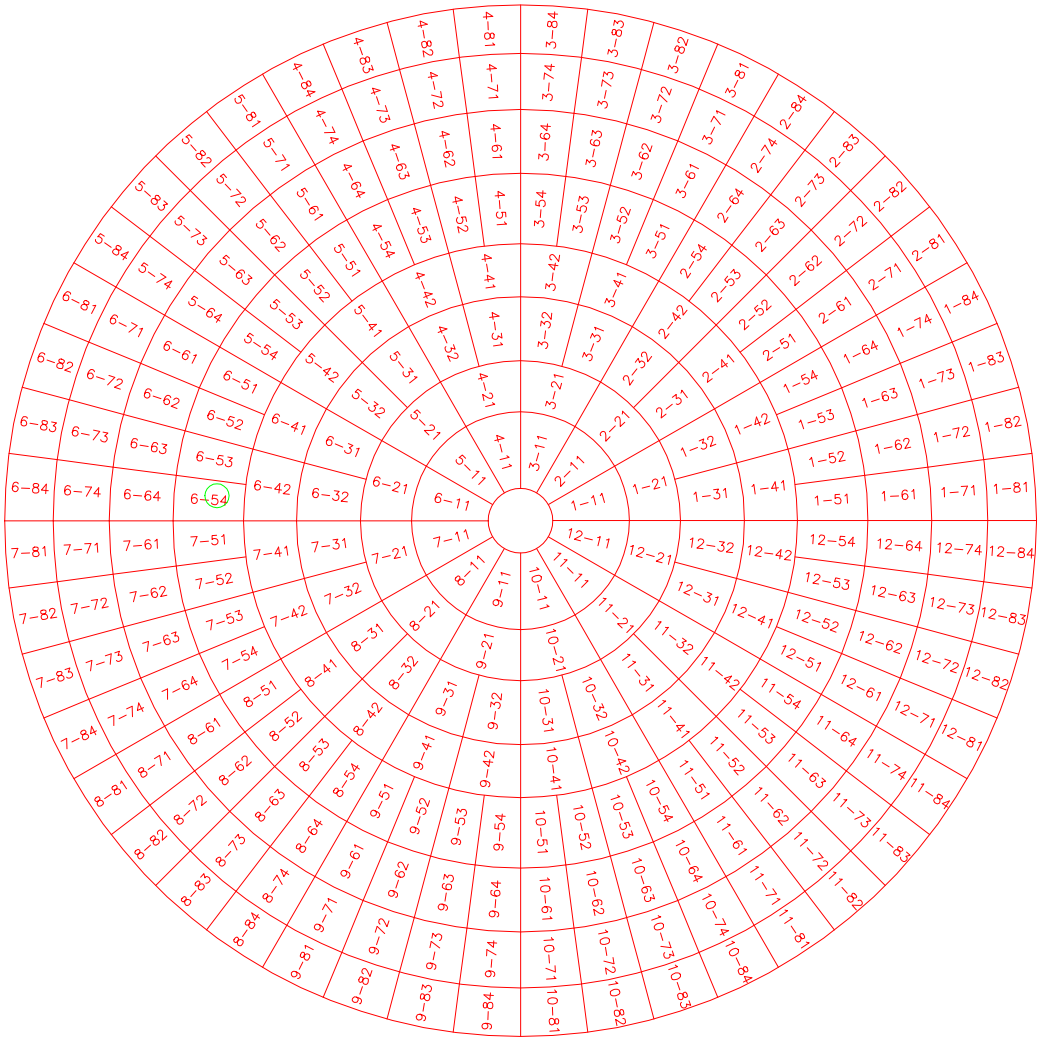

Figure 18: Panel numbering layout for the VertexRSI antenna. The green circle marks the position of the access hole for the optical pointing telescope.

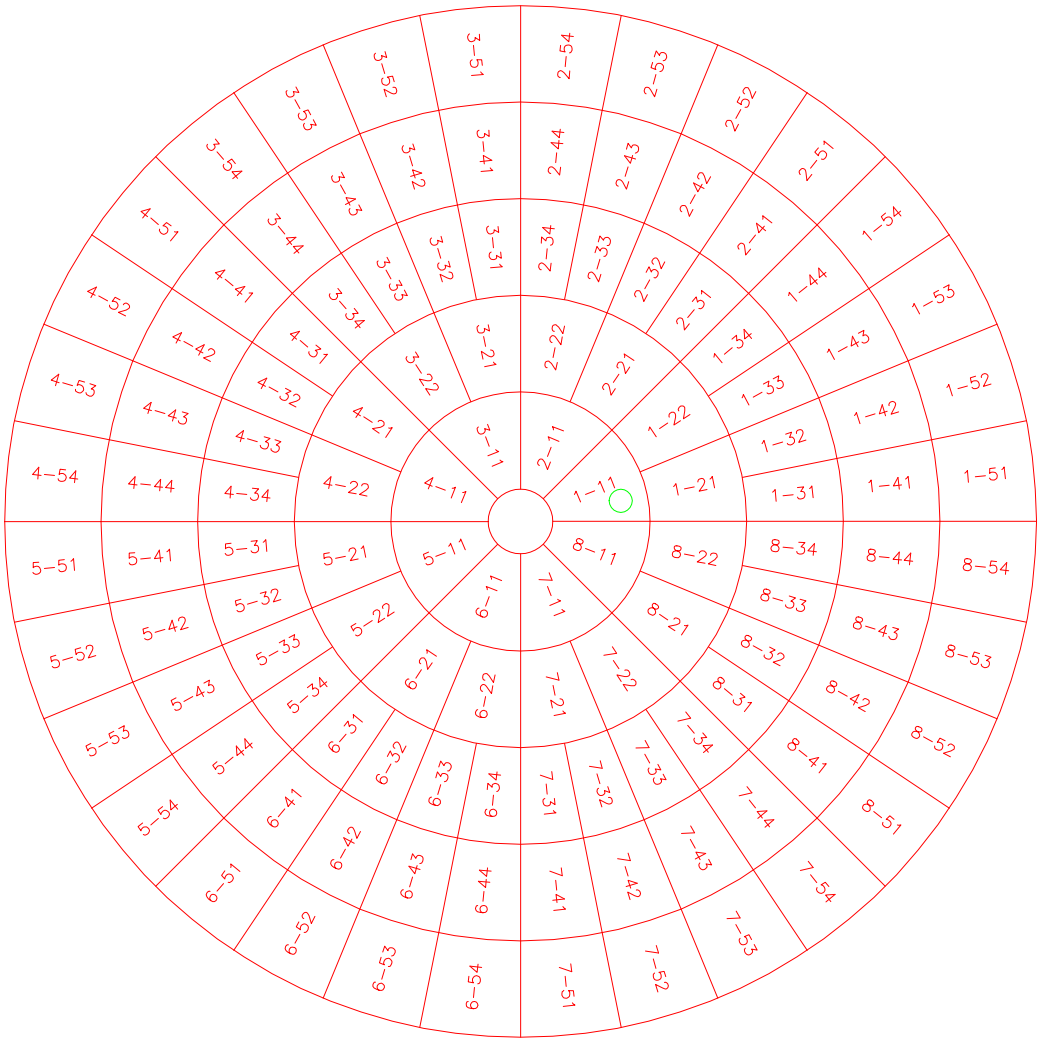

Figure 19: Panel numbering layout for the AEC antenna. The green circle marks the position of the access hole for the optical pointing telescope.

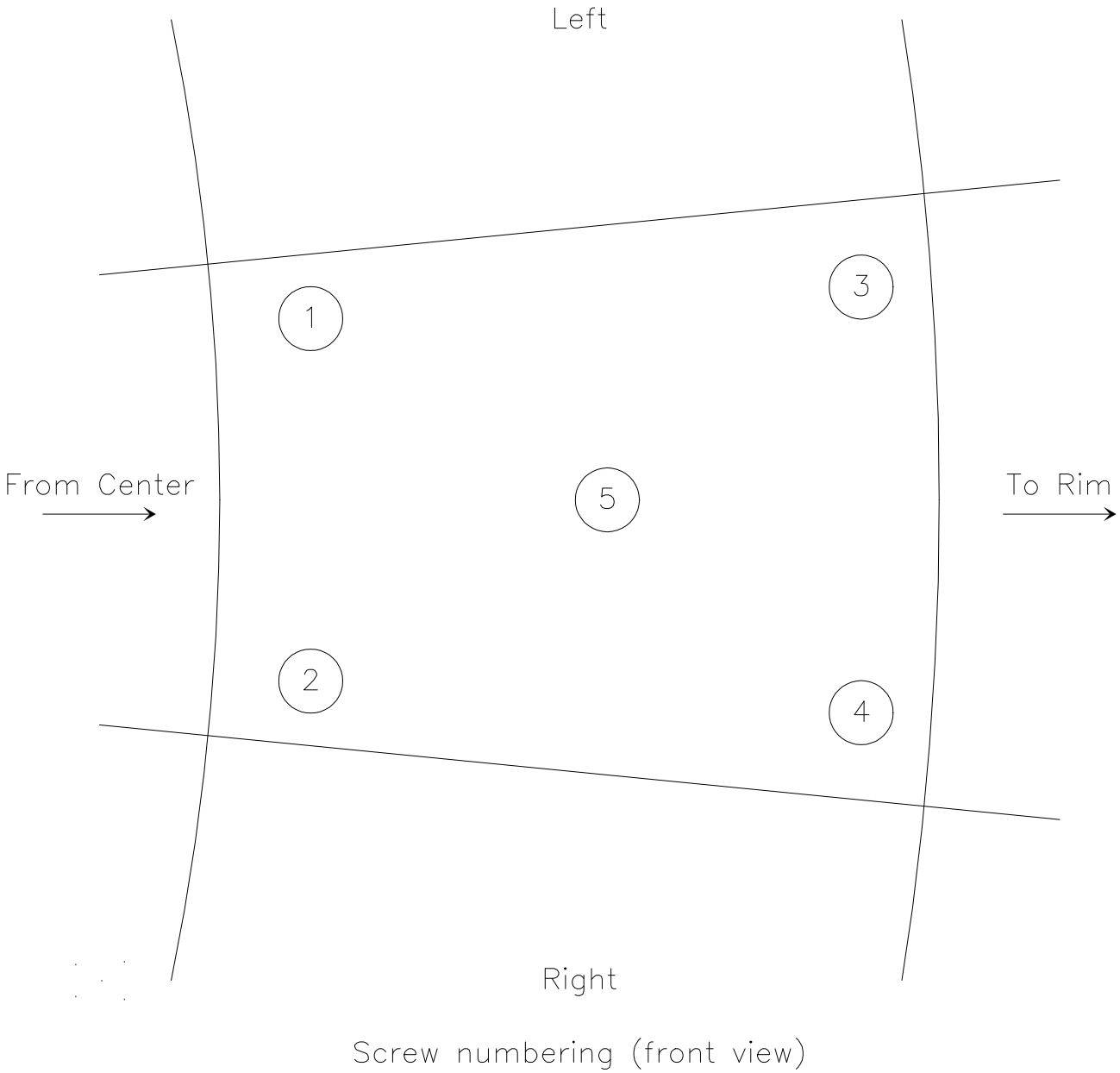

Figure 20: Screw numbering system used for each panel on both the VertexRSI and AEC antennas.

References

Baars, J.W.M., "Dual-Beam Parabolic Antennae in Radio Astronomy", Dissertation Tech. Univ. Delft, 1970

Baars, J.W.M., "Technology of Large Radiotelescopes for Millimeter and Submillimeter Wavelengths", in Infrared and Millimeter Waves, Vol. 9, p .241, Academic Press, 1983

Baars, J.W.M., Hooghoudt, B.G., Mezger, P.G. & de Jonge, M.J., "The IRAM 30-m Millimeter Radio Telescope on Pico Veleta, Spain", A&A, 175, p. 319, 1987

Baars, J.W.M., Greve A., Hein, H., Morris, D., Peñalver, J. & Thum, C., "Design Parameters and Measured Performance of the IRAM 30-m Millimeter Radio Telescope", Proc. IEEE **82**, p. 687, 1994

Baars, J.W.M., Martin, R.N., Mangum, J.G., MeMullin, J. &Peters,W.L.,"The Henrich Hertz Telescope and the Submillimeter Telescope Observatory", PASP, **111**, p. 627,1999

Bennett,J.C., Anderson, A.P., McInnes, P.A. & Whittaker, A.J.T., "Microwave Holographic Metrology of Large Reflector Antennas", IEEE Trans. **AP-24**, p. 295, 1976

Born, M. & Wolf, E., "Principles of Optics", Ch. 8, p. 370, Pergamon Press, 1970

D'Addario, L. R. 1982, "Holographic Antenna Measurements: Further Technical Considerations", NRAO 12-Meter Telescope Memo 202. 1982

Godwin, M.P., Schoessow, E.P. & Grahl, B.H., "Improvement of the Effelsberg 100 Meter Telescope Based on Holographic Reflector Surface Measurement", Astron. Astrophys. **167**, p. 390, 1986

Greve, A., "Reflector Surface Measurements of the IRAM 30-m Radio Telescope", Int. J. Infrared and Millimeter Waves, **7**, p. 121, 1986

Hachenberg,O., Grahl, B.H. & Wielebinski, R., "The 100-m Radio Telescope at Effelsberg", Proc. IEEE, **61**, p. 1288, 1973

Hills, R. *et al*. "High-Resolution Millimetre-Wave Holography on the James Clerk Maxwell Telescope", URSI Assembly Maastricht, 2002

von Hoerner, S., "Design of Large Steerable Antennas", AJ, **72**, p. 35, 1967

Jennison, R., "Radio Astronomy", 1966

Lazareff, B., Carter, M., Halleguen, S., Degoud,L., "Characterization of Holography Horns for ALMA Prototype Antennas", IRAM internal report, 2003

Lucas, R., Glendenning, B. 2001, "ALMA Test Interferometer Raw Data Format", ALMA Software memo 15

Moore, C. M. 1982, "Technical Considerations for Holographic Measurement of the NRAO 12-Meter Surface", NRAO 12-Meter Telescope Memo 174.

Morris, D., "Phase Retrieval in the Radio Holography of Reflector Antennas and Radio Telescopes", IEEE Trans. **AP-33**, p. 749, 1985

Morris, D., Baars, J.W.M., Hein, H., Steppe, H., Thum,C. & Wohlleben, R., "Radioholographic Reflector Measurement of the 30-m Millimeter Radio Telescope at 22 GHz With a Cosmic Signal Source", A&A **203**, p. 399, 1988

Rusch, W.V.T. &Potter, P.D., "Analysis of Reflector Antennas", Academic Press, 1970

Ruze, J., "Antenna Tolerance Theory", Proc. IEEE, **54**, p. 633, 1966

Scott, P. F. & Ryle, M. 1977, "A Rapid Method of Measuring the Figure of a Radio Telescope Reflector", MNRAS, 178, 539.

Silver, S., "Microwave Antenna Theory and Design", MIT Rad.Lab. Series Vol.12, 1949